AN ABSTRACT OF THE THESIS OF

Joshua A. Russell for the degree of Master of Science in Physics presented on February 24, 2011.

Title: Measurement of Optical Bandgap Energies of Semiconductors

Abstract approved: _____

David H. McIntyre

A method for bandgap energy determination using diffuse reflection is presented and compared to the traditional integrating sphere method. We have found the bandgap energies of ZnO, TiO_2, Cu_2O, Si, $SnZrS_3$, $SnZrSe_3$, Sn_2S_3, and BiCuOSe powders with both methods and found they agree within 0.03 eV. We have measured scattering from powder material in the infrared region of the spectrum with a linear wavelength dependence. We have measured optical bowing of the bandgap energies of the $SnZrS_{3-x}Se_x$ system. We also describe in depth the Ocean Optics spectrometer and its components.

Measurement of Optical Bandgap Energies of Semiconductors

by

Joshua A. Russell

A THESIS

submitted to

Oregon State University

in partial fulfillment of
the requirements for the
degree of

Master of Science

Presented February 24, 2011
Commencement June 2011

Master of Science thesis of Joshua A. Russell presented on February 24, 2011.

APPROVED:

Major Professor, representing Physics

Chair of the Department of Physics

Dean of the Graduate School

I understand that my thesis will become part of the permanent collection of Oregon State University libraries. My signature below authorizes release of my thesis to any reader upon request.

Joshua A. Russell, Author

ACKNOWLEDGEMENTS

I would like to thank Janet Tate and David McIntyre for being my advisors and the many helpful and in depth conversations. I would also like to thank Annette Richards who prepared all the material samples and material characterization. Andriy Zakutayev mentored me on the measurement and growth techniques of a solid state lab. And finally, I thank my family for allowing me to follow my calling in life.

CONTRIBUTION OF AUTHORS

Annette Richards prepared all the powder samples, lattice spacing measurements, and material identification with XRD. Janet Tate and David McIntyre were involved in interpretation of the data and design of this thesis.

TABLE OF CONTENTS

Page

1 Introduction 1

2 General Overview of Optical Spectroscopy 2
- 2.1 Transmission and Reflection Measurements . . . 2
- 2.2 Transmission and Reflection Theory . . . 4
  - 2.2.1 Transmission and Reflection of Single Crystals . . . 6
  - 2.2.2 Transmission and Reflection of Thin Films . . . 8
  - 2.2.3 Diffuse Reflection of Powdered Samples . . . 10
- 2.3 Absorption of a Material . . . 11
  - 2.3.1 Absorption of Single Crystals and Thin Films . . . 12
  - 2.3.2 Absorption of Powder Sample . . . 14
- 2.4 Bandgap Energy of a Material . . . 17

3 Spectrometer 21
- 3.1 Ocean Optics Instruments . . . 21
  - 3.1.1 Transmission and Reflection Measurements . . . 23
  - 3.1.2 Diffuse Reflection Measurements . . . 26
  - 3.1.3 Spectrometers . . . 28
  - 3.1.4 Light Sources . . . 37
  - 3.1.5 Shutter System . . . 40
  - 3.1.6 Optical Cages . . . 42
  - 3.1.7 OO STAN-SSH Reflection Standard . . . 48
- 3.2 Scanning Monochromator . . . 51

4 Bifurcated Fiber Method for Measurement of Bandgap Energy 53
- 4.1 Bandgap Energy Calculations . . . 54
- 4.2 Bandgap Comparison . . . 58
- 4.3 Scattering Problem . . . 62
- 4.4 Optical Bowing . . . 69

5 Conclusion 71

TABLE OF CONTENTS (Continued)

Page

Bibliography 72

LIST OF FIGURES

Figure		Page
2.1	The transmission and reflection of light at a single interface.	5
2.2	The transmission and reflection of light at a two interface system.	7
2.3	The transmission and reflection of light in a thin film, substrate system.	9
2.4	The light flux inside of a diffusely reflecting material.	11
2.5	All the expressions for $T/(1-R)$ gives us approximately the same result for the absorption spectrum. Here $T/(1-R)_{Exact}$ is the plot of $T/(1-R)$ as defined in equation 2.17.	14
2.6	The electron path for direct and indirect transitions.	19
2.7	The band gap measurement of TiO_2 powder. We can see band gap is approximately 3.25 eV.	20
3.1	The Ocean Optics spectrometers' layout.	22
3.2	The Ocean Optics spectrometer's transmission measurement light path.	24
3.3	The Ocean Optics spectrometer's transmission cage reflection measurement set up.	25
3.4	The Ocean Optics spectrometer's reflection cage reflection measurement set up.	26
3.5	The Ocean Optics spectrometer's diffuse reflection set up. 1) Bifurcated Optic Fiber 2) Ceramic Sample Holder Cup 3) Sample Material 4) Angular Alignment Apparatus	27
3.6	The internal workings of the Ocean Optics HR4000 spectrometer. The figure from Ocean Optics HR4000 and HR4000CG-UV-NIR Series High-Resolution Fiber Optic Spectrometers: Installation and Operation Manual. 1) SMA connector 2) Slit 3)Filter 4) Collimating Mirror 5) Grating 6) Focusing Mirror 7) L2 Detector Collection Lens 8) CCD Array	29

LIST OF FIGURES (Continued)

Figure | Page

3.7 The slit of the Ocean Optics spectrometer is offset from the center of the bifurcated fiber optic cable. Rotation of the fiber optic cable will change the intensity of light that enters the spectrometer. . . . 31

3.8 The systematic noise of the HR4000 starts when the integration time is set to 3.799 ms and the whole spectrum, from 200 nm to 1100 nm, has the noise when we reach 1.350 ms. 32

3.9 The Ocean Optics NIR256-2.5 spectrometer cools in two different modes. The spectrometer will converge to the set temperature with a sinusoidal with an exponential decay envelope or has a step like function where the temperature will vary by 4 degrees during the measurement. 33

3.10 The Ocean Optics NIR256-2.5 spectrometer has less noise when cooling option is enabled. 35

3.11 The Ocean Optics NIR256-2.5 spectrometer's intensity signals do not increase linearly. After 30 ms the intensity signal no longer increases linearly. 36

3.12 The Ocean Optics DH2000-Bal lamp spectrum measured with the Ocean optics HR4000 spectrometer. 38

3.13 The Ocean Optics HL-2000-FHSA lamp spectrum measured with the Ocean optics NIR256-2.5 spectrometer. 40

3.14 The shutter control circuit. 42

3.15 The transmission cage on the Ocean Optics spectrometer. 44

3.16 The spot size on the transmission cage spectrometer fiber optic needs to be defocused so that you will not get a variation in the signal caused by vibrations of the optical table. 45

3.17 The reflection cage on the Ocean Optics spectrometer. 46

3.18 The peak of the reflection is dependent on the position in the optical cage. The closer the sample is to the lamp fiber optic then the higher the ultraviolet region will be. The infrared region will increase when the sample is further away from the lamp fiber optic. 47

LIST OF FIGURES (Continued)

Figure | Page

3.19 The reflection spectrum of the Ocean Optics STAN-SSH reflection standard measured with the scanning monochromator with the ultraviolet region fitted to the Ocean Optics reflection spectrum and adjusted to a line with the scanning monochromator data. 49

3.20 The map of the surface of the Ocean Optics STAN-SSH reflection standard. We can see that the reflectivity does not change more than the 0.01 percent over the surface of the mirror. The peaks are from the light striking the edge of the mirror. 50

4.1 The diffuse reflectivity of TiO_2 powder. We can clearly see the bandgap onset at about 350 nm. 54

4.2 The absorption spectrum of TiO_2 powder. We assume that the scattering coefficient is constant over this wavelength region. 55

4.3 The bandgap energy of TiO_2 powder is found by plotting $(F(R)\omega\hbar)^{\frac{1}{2}}$ against $\omega\hbar$ and fitting the linear part of the spectrum at the onset. 56

4.4 The diffuse reflectance of Sn_2S_3 powder. 57

4.5 The bandgap energy of Sn_2S_3 powder is found by plotting $(F(R)\omega\hbar)^{\frac{1}{2}}$ against $\omega\hbar$ and fitting the linear part of the spectrum at the onset. 58

4.6 The diffuse reflectance of TiO_2 measured with the bifurcated fiber method and the integrating sphere method. We can see that they are basically the same. 59

4.7 The diffuse reflectance of Sn_2S_3 measured with the bifurcated fiber method and the integrating sphere method. We can see that they are basically the same. 60

4.8 Bandgap energies of 7 powdered samples taken with the bifurcated fiber optic method and the integrating sphere method. 61

4.9 Diffuse reflection and transmission spectra of Si powder. Both the transmission and diffuse reflection spectra were measured with an integrating sphere. 64

4.10 Si powder viewed under 100 times magnification. The powder particles range from 1 micron to 10 micron sizes. 65

LIST OF FIGURES (Continued)

Figure Page

4.11 The diffuse reflection of Si powder before and after being ground in a stone crucible. We see that the smaller the particle size the steeper the baseline absorption slope. 66

4.12 Diffuse reflection of Si powder with the powder thickness ranging from 0.32 mm to 2.25 mm. We see no change in the baseline absorption slope as the thickness changes. 67

4.13 Diffuse reflection of Si crystal with the different surface roughness. We see an increase in the baseline absorption slope as the roughness increases. 68

4.14 Optical bowing of the $SnZrS_{3-x}Se_x$ system. The bandgap energy drops down quickly when $x < 1$. While $x > 1$, the bandgap energy looks to change linearly. 70

DEDICATION

To my wife Erin and my two little monkeys, Josh and Brook.

Chapter 1 – Introduction

A method for bandgap energy determination using diffuse reflection is presented and compared to the traditional integrating sphere method. With the integrating sphere method, the diffuse reflection measurement would take from 15 minutes to 1 hour with the scanning monochromator. We saw a need to shorten the diffuse reflection measurement time. The Ocean Optics spectrometer was built to speed up the transmission and reflection measurement time to less than one second. We developed the bifurcated fiber optic method to measure the diffuse reflection of diffusely reflective materials.

We will first look at the theory behind transmission, specular reflection, and diffuse reflection spectroscopy. Then we present an in-depth look at the Ocean Optics spectrometer and the measurement procedure. Then we will compare the diffuse reflection measurements of the bifurcated fiber method and integrating sphere method. We have found the bandgap energies of ZnO, TiO_2, Cu_2O, Si, $SnZrS_3$, $SnZrSe_3$, Sn_2S_3, and BiCuOSe with both methods and found that these two methods agree within 0.03 eV. We will also consider the scattering from powdered material in the infrared region of the spectrum with a linear wavelength dependence. Finally, we measured the optical bowing of bandgap energies of the $SnZrS_{3-x}Se_x$ system. We also describe in depth the Ocean Optics spectrometer and its components.

Chapter 2 – General Overview of Optical Spectroscopy

The discovery of the sun's light being made up of a spectrum of wavelengths by Isaac Newton in 1666 was the first step in the use of spectroscopy to characterize materials [1]. It was not until the early 1800's that Kirchhoff discovered that each element and compound has its own unique spectrum which could be used to identify the material [1]. Bandgaps are one of the most important properties of modern semiconductors. With applications in photovoltaics, microprocessing, visual display, and lighting sources, the bandgap of a semiconductor is an important property for designing and discovering new applications for semiconductors.

2.1 Transmission and Reflection Measurements

The most common method of determining the bandgap of a semiconductor is by optical measurements. To measure the bandgap, we first measure the transmission and reflection of a thin film or single crystal or the diffuse reflection of a powder.

To measure the transmission of a sample we expose the sample to light which travels in the direction that is orthogonal to the surface of the material. We then collect the light that is transmitted or goes through the sample. We do the same for the reflection of a sample except we collect the light that reflects off the surface or changes direction by 180 degrees at the vacuum material interface. We will

call the light that changes direction by 180 degrees the specular reflection. For the diffuse reflection measurements we collect all the light that is reflected off of a sample except the specular reflected light. The transmission and reflection are defined as the ratio of the transmitted or reflected light's intensity to the incident light's intensity.

$$T_{Sample}(\lambda) = \frac{S_{Sample}(\lambda)}{S_{Reference}(\lambda)} \tag{2.1}$$

$$R_{Sample}(\lambda) = \frac{S_{Sample}(\lambda)}{S_{Reference}(\lambda)} \tag{2.2}$$

Here $T_{Sample}(\lambda)$ is the transmittance of a material and $R_{Sample}(\lambda)$ is the reflectivity of a material. Both T and R are bound between 0 and 1. $S_{Sample}(\lambda)$ is the intensity that has been reflected or transmitted by the sample. $S_{Reference}(\lambda)$ is the intensity that has been reflected or transmitted by a reference. The reference needs to have 100 percent reflection or transmission coefficients to measure the absolute transmission or absolute reflectivity.

In practice it is difficult to have the ideal conditions to use equations 2.1 and 2.2. There is background light that is detected when the light source is blocked and it is difficult to get a reflection standard that is 100 percent reflective or has an uniform reflectivity for all wavelengths. To correct for the background radiation we take an additional measurement with the lamp off or blocked so there is no incident light on the sample. We then record the intensity and call this value the background intensity. The background intensity includes the ambient light and any reflections from the apparatus. To ensure that we get 100 percent for the

transmission reference, we allow the incident light to go straight to the detector. We use the vacuum as our transmission reference. When using a reflection reference sample we need to know the reflectivity of the reference at each wavelength so we can normalize the reflection.

$$T_{Sample}(\lambda) = T_{Reference}(\lambda) \frac{S_{Sample}(\lambda) - S_{Background}(\lambda)}{S_{Reference}(\lambda) - S_{Background}(\lambda)} \tag{2.3}$$

$$R_{Sample}(\lambda) = R_{Reference}(\lambda) \frac{S_{Sample}(\lambda) - S_{Background}(\lambda)}{S_{Reference}(\lambda) - S_{Background}(\lambda)} \tag{2.4}$$

Here $R_{Reference}(\lambda)$ or $T_{Reference}(\lambda)$ is the reflectivity or transmittance of a reference. $S_{Background}(\lambda)$ is the intensity that is measured when the light source is blocked for transmission and reflection. We subtract the background intensity from each of the reference's and sample's intensities. We also multiply the transmittance or reflectance of our sample by a reference transmittance or reflectance so we will get the correct absolute transmission and absolute reflection. In practice the reference transmittance is 1 for all wavelengths when using the vacuum as the transmission reference. For reflection the reference reflectivity is supplied by a mirror or material with a known reflectivity at each wavelength that has been measured.

2.2 Transmission and Reflection Theory

For single interface transmission and reflection we define the light as plane waves. We assume the k vector is orthogonal to the surface of the interface so we would

say that $\theta = 0$.

$$E = E_0 e^{i(kr-\omega t)} \tag{2.5}$$

Here E is the electric field, ω is the angular frequency, k is the wave number, r is the position vector amplitude, and t is time [2]. We also assume that the index of refraction is complex.

$$N_i = n_i + i\kappa_i \tag{2.6}$$

Here N is the complex index of refraction, n is the real coefficient of the index of refraction, and κ is the imaginary coefficient of the index of refraction.

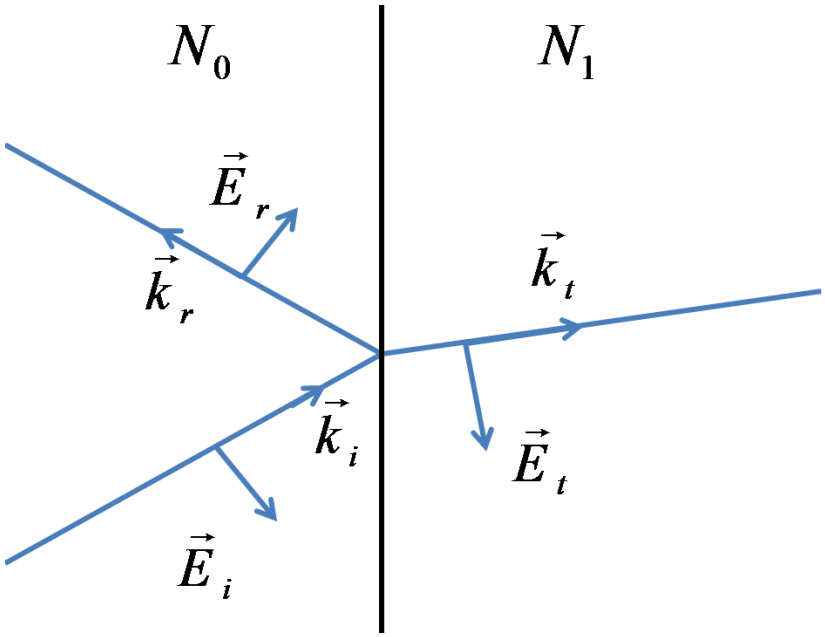

Figure 2.1: The transmission and reflection of light at a single interface.

For a single interface we use E and B field boundary conditions at the interface to derive the Fresnel equations with the incident angle set to 0 [2]. The intensity reflection and transmission coefficients are,

$$R_{01} = \frac{(n_0 - n_1)^2 + {\kappa_1}^2}{(n_0 + n_1)^2 + {\kappa_1}^2} \tag{2.7}$$

$$T_{01} = \frac{4n_0 n_1}{(n_0 + n_1)^2 + {\kappa_1}^2} \tag{2.8}$$

where we define the 01 interface as the interface between material 0 and material 1 in figure 2.1.

2.2.1 Transmission and Reflection of Single Crystals

For a single crystal we use a two interface system where the thickness of the single crystal is defined as d. In figure 2.2, we see the ray diagram of the light path through the single crystal.

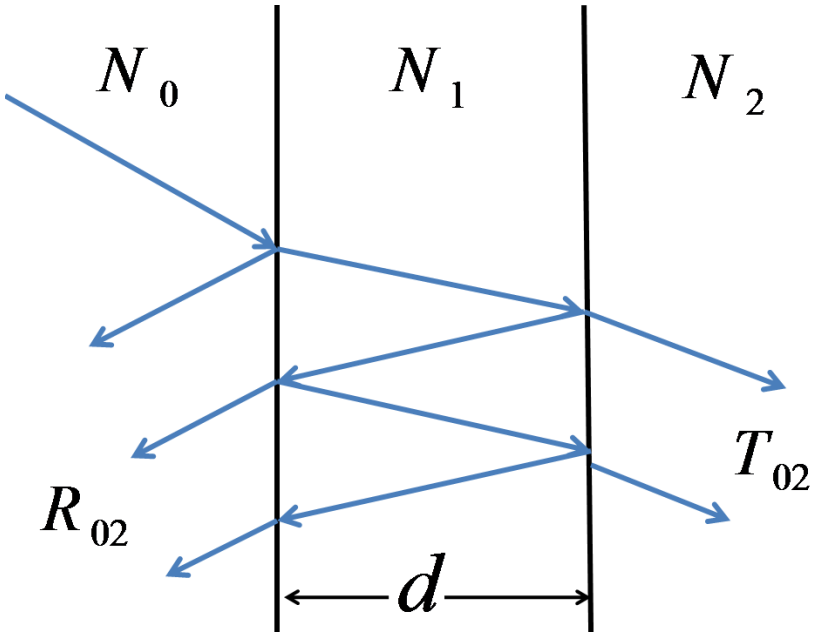

Figure 2.2: The transmission and reflection of light at a two interface system.

There are two cases: when d is greater than the coherence length of the incident light and when d is less than the coherence length. For the case where d is less than the coherence length, there is interference between the multiple reflections and transmissions. Using a geometric argument, we arrive at equation 2.9 for reflection and equation 2.10 for transmission of a single crystal [3].

$$R_{02} = \left| r_{01} + \frac{r_{12} t_{01} t_{10} e^{-\alpha d} e^{i\delta}}{1 - r_{10} r_{12} e^{-\alpha d} e^{i\delta}} \right|^2 \tag{2.9}$$

$$T_{02} = \frac{n_2}{n_0} \left| \frac{t_{01} t_{12} e^{-\frac{\alpha d}{2}} e^{i\frac{\delta}{2}}}{1 - r_{10} r_{12} e^{-\alpha d} e^{i\delta}} \right|^2 \tag{2.10}$$

Where the amplitude transmission and reflection coefficients are

$$t_{mn} = \frac{2N_m}{N_m + N_n}$$
$$r_{mn} = \frac{N_m - N_n}{N_m + N_n}$$
$$\delta = \frac{4\pi n_1 d}{\lambda}$$

We define R_{02} and T_{02} as the reflection and transmission from both the first and second interface. For the case where d is greater than the coherence length we have to average over all phases and come to the result for transmission and reflection for the single crystal [4].

$$R_{02} = R_{01} + \frac{R_{12}T_{01}T_{10}e^{-2\alpha d}}{1 - R_{10}R_{12}e^{-2\alpha d}} \tag{2.11}$$
$$T_{02} = \frac{T_{01}T_{12}e^{-\alpha d}}{1 - R_{10}R_{12}e^{-2\alpha d}} \tag{2.12}$$

Where

$$T_{mn} = \frac{n_n}{n_m}\left|t_{mn}\right|^2$$
$$R_{mn} = \left|r_{mn}\right|^2$$

2.2.2 Transmission and Reflection of Thin Films

When looking at the transmission and reflection of a thin film on a substrate we need to consider a 3 interface system, as shown in figure 2.3. We will assume

that the substrate's thickness is much larger than the coherence length of the light while the thin film's thickness is less than the coherence length of the light. We also assume that there is no absorption from the substrate.

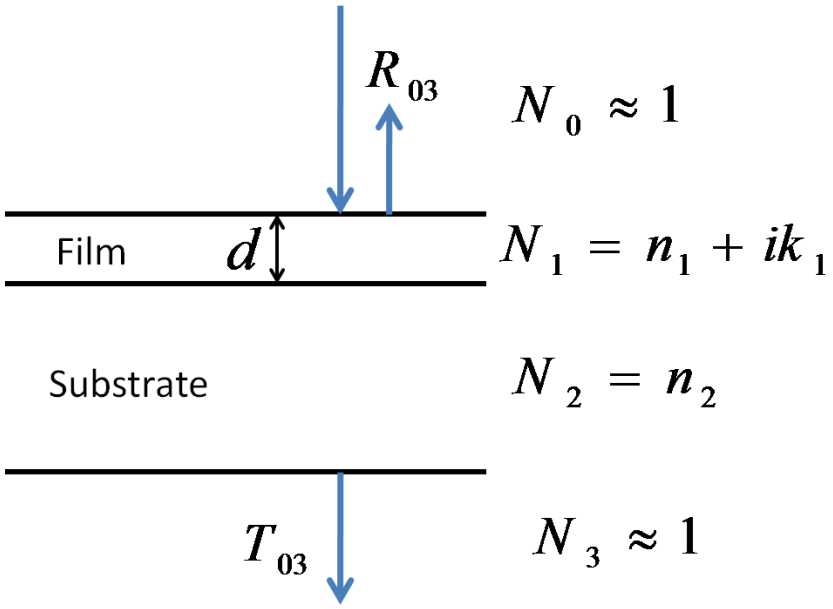

Figure 2.3: The transmission and reflection of light in a thin film, substrate system.

We can model the three-interface system as a two-interface system by using equations 2.11 and 2.12 with the air-crystal interface replaced by a complex reflection and transmission that accounts for the thin film [3].

$$R_{03} = R_{02} + \frac{R_{23}T_{02}T_{02}}{1 - R_{02}R_{23}} \tag{2.13}$$

$$T_{03} = \frac{T_{23}T_{02}}{1 - R_{20}R_{23}} \tag{2.14}$$

We define R_{03} and T_{03} as the reflection and transmission from all 3 interfaces. Now

the air-crystal interface, 01 and 10 in figure 2.2, is replaced by the complete air-film-substrate system as a single interface, 02 and 20 in figure 2.3. The crystal-air interface, 12 in figure 2.2, is replaced by the substrate-air interface, 23 in figure 2.3.

2.2.3 Diffuse Reflection of Powdered Samples

Diffuse reflection is calculated differently from single crystal and thin film models. With powder material we model the light as a flux instead of a plane wave. We define a flux as the upward or downward intensity that is travelling through a section of material of thickness dz [5]. Kubelka Munk theory uses two fluxes, an upward flux which we will call $J(z)$ and a downward flux which we will call $I(z)$, as shown in figure 2.4. We define the diffuse reflectance as $J(z)$ where $z > d$. We will take a closer look at diffuse reflection when we consider the absorption of a material.

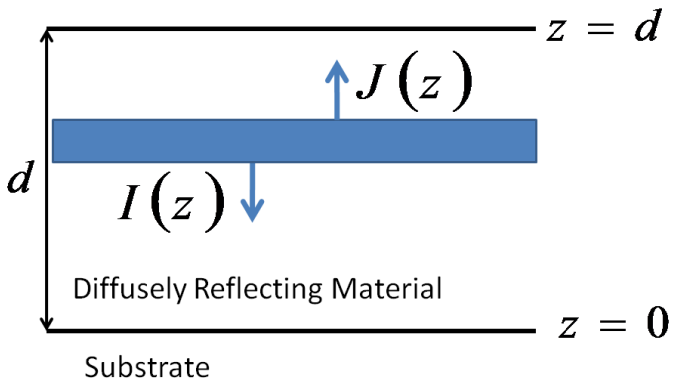

Figure 2.4: The light flux inside of a diffusely reflecting material.

2.3 Absorption of a Material

Once we measure the transmission or reflection of a thin film, single crystal, or powder sample we are now able to calculate the absorption of the material. Here we are talking about the absorption and not the absorptance of a material. Absorption is the light that enters the material and does not leave while, absorptance can also include scattering and other processes that does not absorb the light into the material. Absorptance is defined as all the light that is not specularly reflected or transmitted [2].

$$A = 1 - T - R \tag{2.15}$$

We define absorption in terms of wavelength and the imaginary coefficient of the index of refraction [2].

$$\alpha = \frac{2\omega\kappa}{c} = \frac{4\pi\kappa}{\lambda} \tag{2.16}$$

Here c is the speed of light in a vacuum, and λ is the wavelength of light. It is important to remember that κ is a function of λ.

2.3.1 Absorption of Single Crystals and Thin Films

While finding the absorption of the single crystal or thin film sample, it is convenient to look at the transmission divided by one minus the reflection. This expression eliminates the fringes from multiple reflection interference [3]. We can see from equations 2.9 and 2.10 that the absorption coefficient can be determined directly from the transmission and reflection of the single crystal and thin film systems. We start by using equations 2.14 and 2.13 [3].

$$\left(\frac{T}{1-R}\right)^{-1} = \frac{1-R_{02}}{T_{23}T_{02}} - \frac{R_{23}}{T_{23}}\left(R_{20}\frac{1-R_{02}}{T_{02}} + T_{20}\right) \tag{2.17}$$

If we assume R_{23} is less than 5 percent as with glass substrate in the visible and infrared regions of the spectrum and if $R_{02} + T_{02} < 1$, then the second term in equation 2.17 can be neglected. This gives us a simpler expression for finding the

absorption [3].

$$\frac{T}{1-R} = \frac{T_{23}T_{02}}{1-R_{02}} \tag{2.18}$$

Now we can solve for α if we know n_1 and d with an iterative calculation.

To see how equation 2.18 relates to the film absorption, assume that the film absorption is small, which leads to a simpler expression of equation 2.18 [3].

$$\frac{T}{1-R} = \frac{|t_{12}|^2 |t_{23}|^2}{e^{\alpha d} - e^{-\alpha d} |r_{12}|^2} \tag{2.19}$$

If we ignore the effect of the back side of the substrate, assume $R_{23} < 5$ percent, then we get

$$\frac{T}{1-R} = e^{-\alpha d} \tag{2.20}$$

which is Beer's law [6]. In figure 2.5, we have plotted three expressions, 2.17, 2.19, 2.20, for $T/(1-R)$. This plot shows that all three expressions for $T/(1-R)$ are about the same.

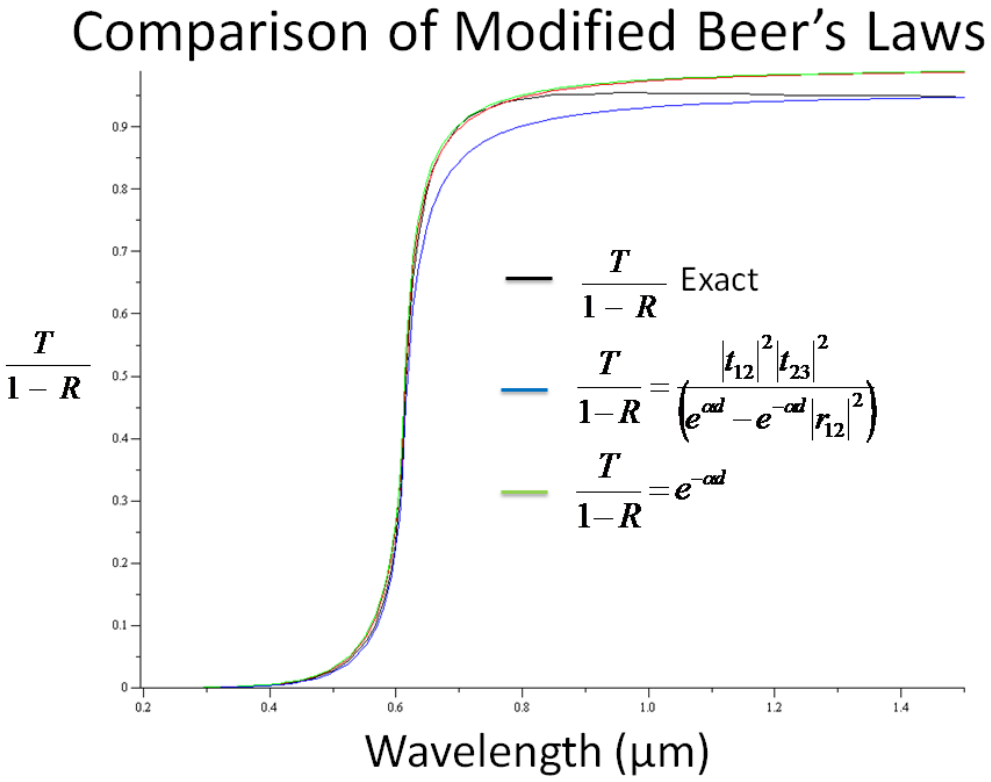

Figure 2.5: All the expressions for $T/(1-R)$ gives us approximately the same result for the absorption spectrum. Here $T/(1-R)_{Exact}$ is the plot of $T/(1-R)$ as defined in equation 2.17.

2.3.2 Absorption of Powder Sample

Powder samples can not use the same method as the single crystals and thin films do to calculate the absorption of the material. We use Kubelka Munk theory to model the diffuse reflection of the powder sample as explained in section 2.2.3. We

also define the absorption coefficient as k and the scattering coefficient as s. For isotropic scattering and monoenergetic radiation, we have the scalar equation of transport with azimuthal symmetry and planar geometries shown in equation 2.21 [7].

$$u\frac{\partial\Phi(z,u)}{\partial z} = -(k+s)\Phi(z,u) + \frac{s}{2}\int_{-1}^{1}\Phi(z,u')\,du' \tag{2.21}$$

Where

$$u = cos(\theta)$$

Now we define the distribution function, as shown in figure 2.4, $J(z)$ is in the upward direction and $I(z)$ in the downward direction.

$$\Phi(z,u) = \Theta(-u)I(z) + \Theta(u)J(z) \tag{2.22}$$

Here Θ is the heavy sided step function. When we plug the distribution function into equation 2.21, we find the two equations for the change in $J(z)$ and $I(z)$ [7].

$$\frac{dJ(z)}{dz} = -(k+s)J(z) + s(I(z)) \tag{2.23}$$

$$\frac{dI(z)}{dz} = (k+s)I(z) - s(J(z)) \tag{2.24}$$

Combining these equations we get a combined expression for both $J(z)$ and $I(z)$ 2.25.

$$\frac{1}{s}\frac{dr(z)}{dz} = r(z)^2 - 2(2a-1)r(z) + 1 \tag{2.25}$$

Where

$$r(z) = \frac{J(z)}{I(z)}$$
$$a = \frac{k+s}{s}$$

Now if we assume we are outside of the material, we can see that there is no change in the ratio $r(z)$ and that the ratio will remain the same no matter where we are outside of the material. This leads us to the equation for the absorption when solving equation 2.25 for a.

$$a = \frac{(1+R_\infty)^2}{4R_\infty} \tag{2.26}$$
$$f(R_\infty) = \frac{k}{s} = \frac{(1-R_\infty)^2}{4R_\infty} \tag{2.27}$$

Where

$$R_\infty = r(\infty)$$

If we assume that the scattering from the material is constant for the wavelength range we are measuring, then any structure in equation 2.27 is contributed by the

absorption coefficient, k.

2.4 Bandgap Energy of a Material

We have found the absorption coefficient in terms of the diffuse reflectance. Now we need to relate the diffuse reflection to the bandgap energy. We start by looking at the relation between the complex permittivity, ε, and the complex index of refraction, N [8].

$$\varepsilon = N^2 \tag{2.28}$$

In equation 2.16, we found the relation between the absorption coefficient and the imaginary coefficient of the index of refraction. Using equation 2.29 we can relate the absorption coefficient to the imaginary coefficient of the permittivity.

$$\kappa = \frac{\alpha\lambda}{4\pi} = \frac{\varepsilon_i}{n} \tag{2.29}$$

$$\frac{\alpha}{\omega\hbar} = \frac{\varepsilon_i}{n} * C \tag{2.30}$$

Here n and κ are defined in equation 2.6, λ is the wavelength, ε_i is the imaginary coefficient of the permittivity, $\omega\hbar$ energy of the photon, and C is a constant. The imaginary coefficient of the permittivity is related to the joint density of states [9].

$$\epsilon_i = C_1 \frac{1}{\omega^2} |P_{cv}| D_j \tag{2.31}$$

Where we define the joint density of states, D_j, and the transition matrix element, P_{cv}, as

$$D_j = \frac{1}{4\pi^3} \int \frac{dS_k}{|\nabla_k (E_c - E_v)} \tag{2.32}$$

$$P_{cv} = \langle \psi_c | - e\vec{E} \cdot \vec{r} | \psi_v \rangle \tag{2.33}$$

We define S_k as the constant energy surface for $E_c - E_v$.

Calculating the joint density of states we find an expression for the imaginary coefficient of the permittivity in terms of the bandgap energy [9].

$$\epsilon_i = C_2 \frac{1}{(\omega\hbar)^2} (\omega\hbar - E_{Bandgap})^p \tag{2.34}$$

$$\alpha\omega\hbar = C(\omega\hbar - E_{Bandgap})^p \tag{2.35}$$

Here $\omega\hbar$ is the photon energy, $E_{Bandgap}$ is the optical bandgap energy, p is the bandgap transition dependent exponent, and C is a constant. This equation is only valid as long as the photon energy is greater than the material's bandgap energy. The exponent, p, is dependent on whether the bandgap transition is direct or indirect and whether the transition is allowed or forbidden.

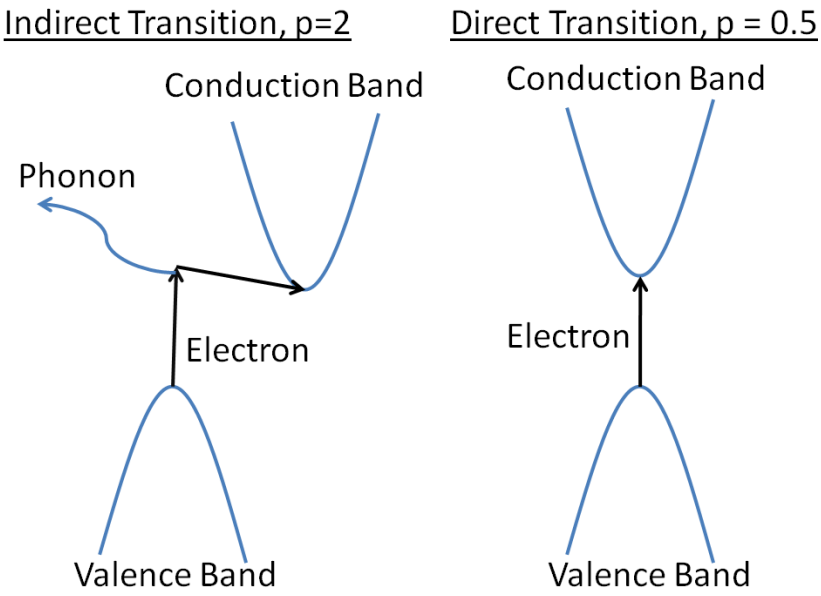

Figure 2.6: The electron path for direct and indirect transitions.

We plot $(\alpha\omega\hbar)^{\frac{1}{p}}$ against $\omega\hbar$ and fit the linear part of the bandgap onset. We can see that when $\alpha = 0$, equation 2.35 says the bandgap energy is equal to the energy of the photon. In figure 2.7, we plot the bandgap measurement for TiO_2 powder. We can see the linear region starts at 3.3 eV and extends to 3.5 eV. We fit the linear region with a line and extend it to the energy axis to find the energy axis intercept. For this sample we can see the band gap is approximately 3.25 eV.

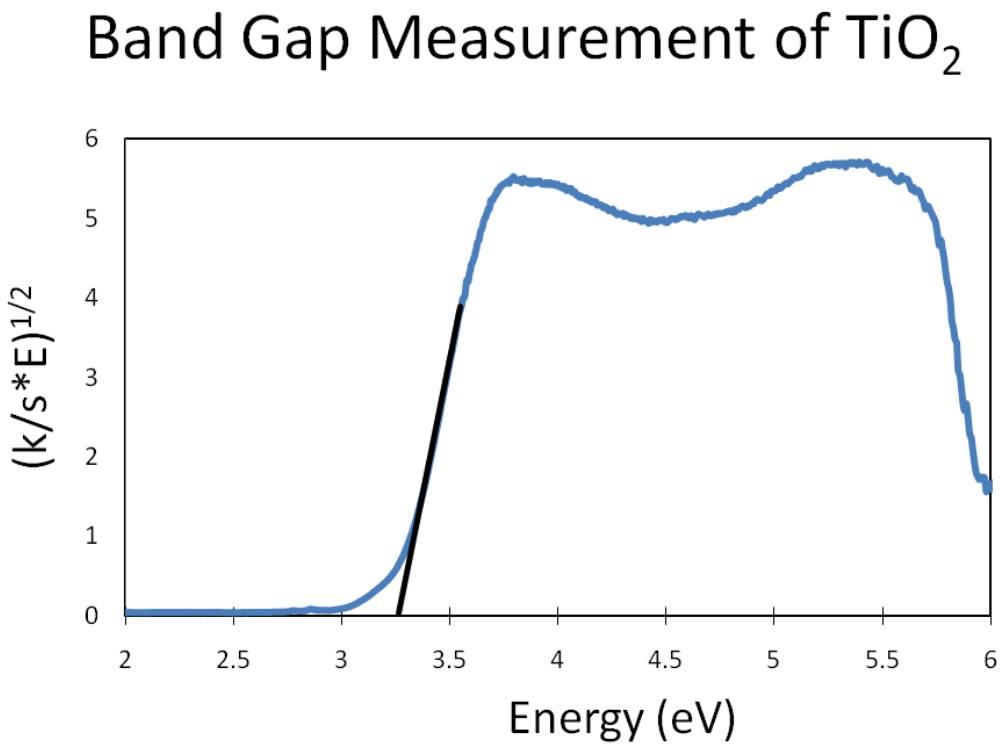

Figure 2.7: The band gap measurement of TiO_2 powder. We can see band gap is approximately 3.25 eV.

Chapter 3 – Spectrometer

In this chapter, we will discuss how we measured the transmission and reflection of single crystals and thin films and the diffuse reflection of powdered samples of semiconductors. We used two different spectrometers to measure the transmission and reflection. The Ocean Optics spectrometer is based on an array detector which separates all the light into individual wavelengths at the same time. The scanning monochromator is based on a monochromator design which exposes the sample to a single wavelength at a time.

3.1 Ocean Optics Instruments

We will first look at the Ocean Optics spectrometer which is made up of 3 components: the spectrometers, lamps, and the fiber optics, as shown in figure 3.1. The Ocean Optics spectrometer is made up of two spectrometers: Ocean Optics HR-4000 and Ocean Optics NIR256-2.5. The HR-4000 measures the ultraviolet-visible region of the spectrum with a wavelength range from 200 nm to 1100 nm. The HR-4000 does this with a grating that separates the wavelengths of light and directs the different wavelengths on to a Toshiba TCD1304AP linear CCD array where the intensity is converted to the spectrum signal. The CCD array has a 14 bit A/D converter with 100 e^- per quanta of signal, called a count, at 800 nm [10].

We found the resolution of the spectrometer to be larger than 0.6 nm and smaller than 2 nm. The Ocean Optics NIR256-2.5 measures the near infrared region of the spectrum with a wavelength range from 850 nm to 2600 nm. The NIR 256-2.5 spectrometer does this with a grating that separates the wavelengths of light and directs the different wavelengths on to a Hamamatsu G9208-256 InGaAs linear array where the intensity is converted to the spectrum signal. The NIR256-2.5 has an optical resolution no smaller than 6.85 nm.

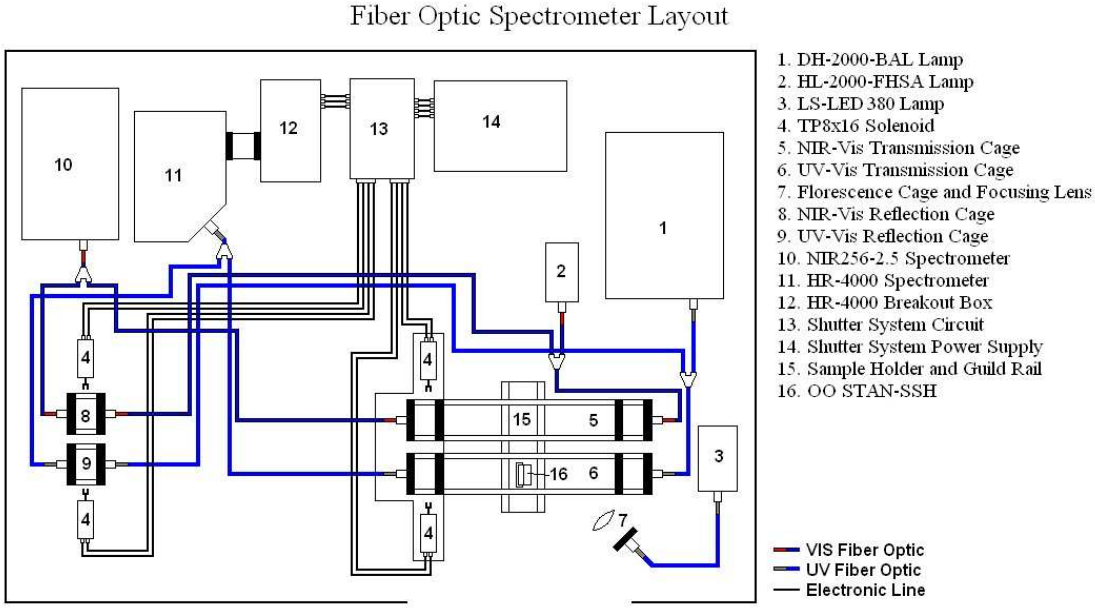

Figure 3.1: The Ocean Optics spectrometers' layout.

The Ocean Optics spectrometer has two light sources. An Ocean Optics Mikropack DH-2000-BAL Deuterium Tungsten Halogen Light Source is used for the ultraviolet-visible measurements and an Ocean Optics Mikropack HL-2000 Tungsten Halogen

Light Source is used for the visible-near infrared measurements. The Ocean Optics Mikropack DH-2000-BAL has a spectral range from 200 nm to 2600 nm. The Ocean Optics Mikropack HL-2000 has a spectral range from 350 nm to 2600 nm.

3.1.1 Transmission and Reflection Measurements

We measure the transmission of a sample by shining white light on the material and collecting the light that is transmitted through the sample. When taking a transmission measurement we mount the sample in the optical cage as shown below in figure 3.2. We first block the light from entering the fiber optic cable that is connected to the spectrometer with the shutters connected to the solenoids, numbered 4 in figure 3.1, on the transmission and reflection cages to take the background spectrum. Next we open the shutter on the transmission cage to allow light to travel to the spectrometer. We take a reference spectrum with the sample removed from the optical cage, with the lamp on, and transmission shutter open. This gives us the reference spectrum to use in transmission calculation. Now we insert the sample into the path of lamp light. We get the sample to be as close to normal with respect to the light path as we can and we take a sample spectrum. The spectrometer's Lab View program averages a chosen number of spectra and then calculates the transmission spectrum with equation 2.3.

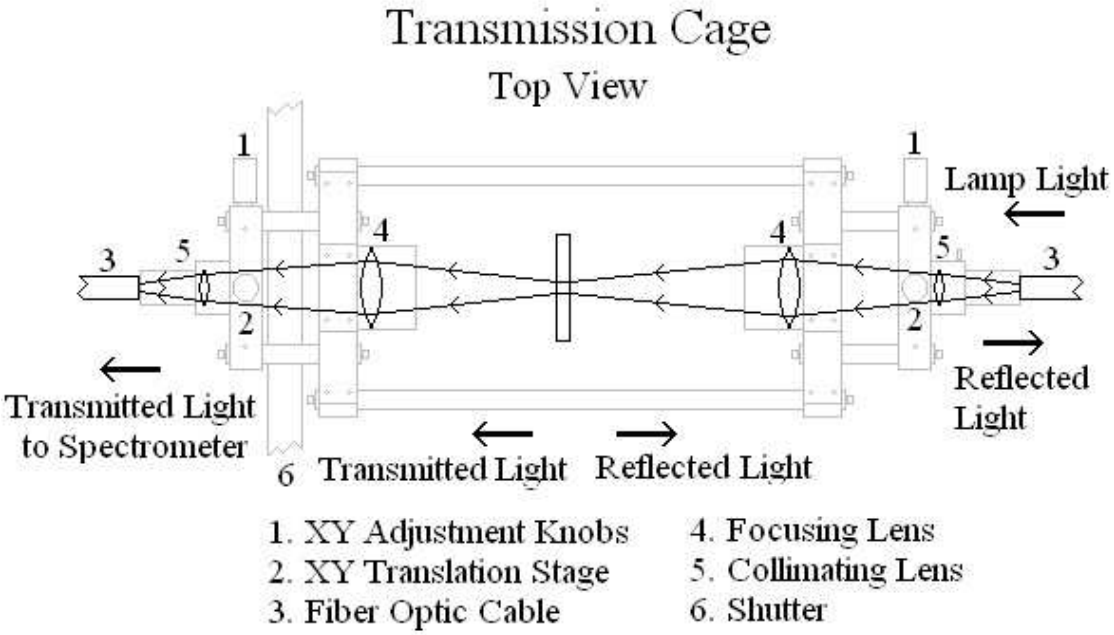

Figure 3.2: The Ocean Optics spectrometer's transmission measurement light path.

We use the same process for measuring the reflection as we do for the transmission except we use a different reference and shutter procedure. The light path for a reflection measurement through the transmission and reflection cages is shown in figures 3.3 and 3.4. For reflection measurements we use Ocean Optics OO STAN-SSH reflection standard. The standard is an aluminium reflection standard mirror and has a known spectral wavelength range from 200 nm to 2600 nm. We first close the shutter on the transmission cage but leave the reflection cage shutter open to allow the reflection of the lenses to be included with the background measurement. With the shutter blocking only the transmission fiber optic cable, we take the background spectrum. Without changing the shutter positions, we place OO

STAN-SSH reflection standard in the path of the light. We maximize the signal of the mirror with an adjustable angular mirror mount. When we have the signal maximized we take the reference spectrum. Now we remove the mirror and we insert the sample into the path of the light. We take a sample spectrum and the spectrometer's Lab View program averages a chosen number of spectra and then calculates the reflection spectrum using equation 2.4.

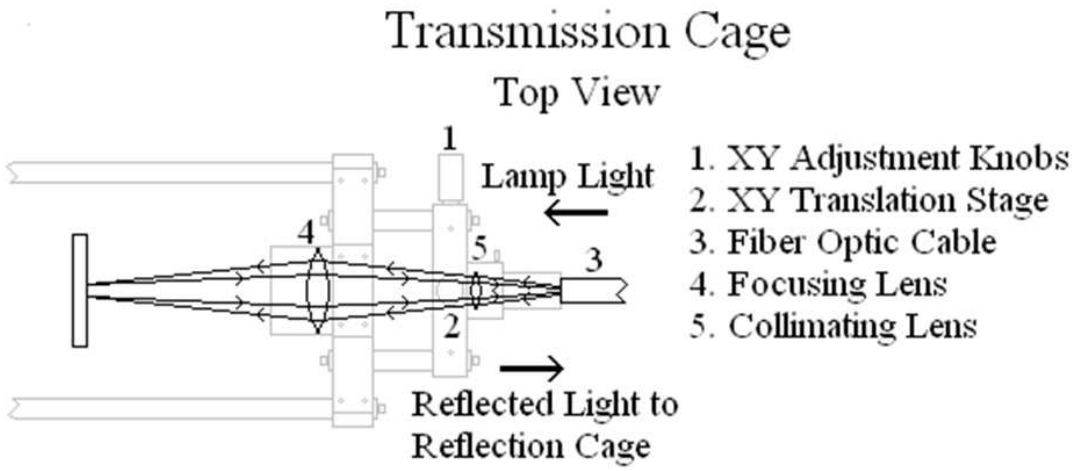

Figure 3.3: The Ocean Optics spectrometer's transmission cage reflection measurement set up.

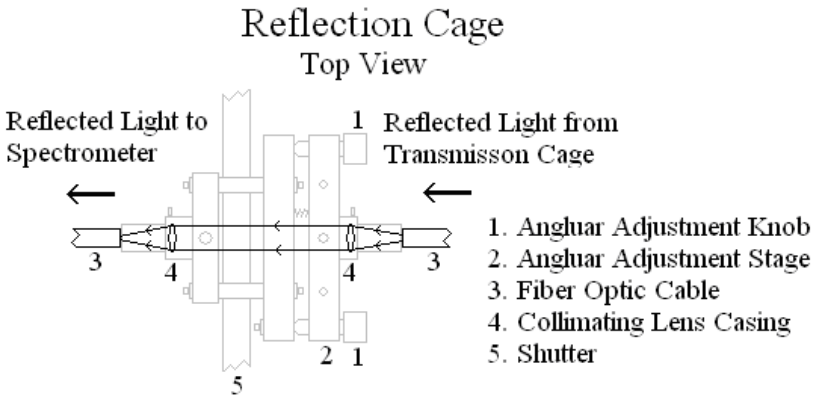

Figure 3.4: The Ocean Optics spectrometer's reflection cage reflection measurement set up.

3.1.2 Diffuse Reflection Measurements

We measure the diffuse reflection of a sample by shining broadband light on a powder material and collecting the light which reflects off of the sample.

The fiber optic spectrometer has the lamp and spectrometer connected to the sample with a bifurcated fiber optic cable, as shown in figure 3.5. The powder sample is placed approximately 3 mm below the double fiber end of the bifurcated fiber optic cable. We used an Ocean Optics QBIF400-VIS/NIR Bifurcated Optical Fiber with a fiber diameter of 400 micron with the visible-near infrared measurement. For the ultraviolet-visible measurement we use an Ocean Optics ZFQ-9803 Bifurcated Optical Fiber with fiber diameter of 455 micron.

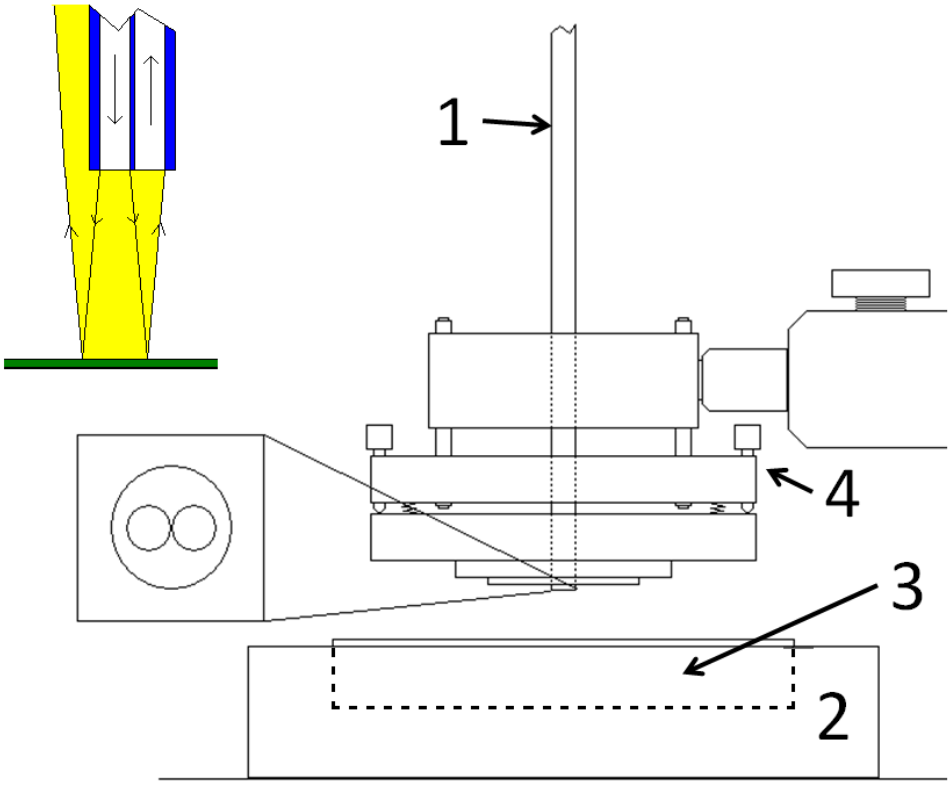

Figure 3.5: The Ocean Optics spectrometer's diffuse reflection set up. 1) Bifurcated Optic Fiber 2) Ceramic Sample Holder Cup 3) Sample Material 4) Angular Alignment Apparatus

When taking a diffuse reflection measurement we mount the sample in a 2.25 mm deep ceramic dish as shown in figure 3.5. We compact the sample into the ceramic dish with a glass slide to give an approximately flat surface. We first remove the sample from below the bifurcated fiber optic. We place a piece of black paper which is angled at approximately 45 degrees from normal of the light

path and record the dark spectrum. Next we place the diffuse reflection standard under the fiber optic cable and adjust the integration time to maximize the signal without saturating the detector. We take a reference spectrum with the reflection standard $BaSO_4$. We assume that the reflection standard is 100 percent reflective. Now we insert the powder sample into the path of light. We get the sample to be as close to normal as we can and we take a sample spectrum. It is important to make the distance between the double fiber end and the sample and the distance between the double fiber end and the reference as close to being the same distance. The spectrometer's Lab View program averages a chosen number of spectra and then calculates the diffuse reflection spectrum with equation 2.4.

3.1.3 Spectrometers

The Fiber Optic Spectrometer uses two spectrometers to make measurments, the HR-4000 in the ultraviolet-visible part of the spectrum and the NIR256-2.5 in the near infrared part of the spectrum.

3.1.3.1 HR-4000

The Ocean Optics HR-4000 spectrometer is made up of a CCD array, SMA connector, 50 micron slit, 200 nm to 1100 nm filter, collimating mirror, and grating [10]. As shown in figure 3.6, the light enters the spectrometer from an input fiber optic cable which is connected to the SMA connector [11]. The light travels through a

slit which is connected to the other end of the SMA connector. The input light then travels through a 200 nm to 1100 nm bandpass filter. A collimating mirror then directs the light onto the grating. This is where the different wavelengths of light are separated and the light is then focused onto the CCD array with a focusing mirror.

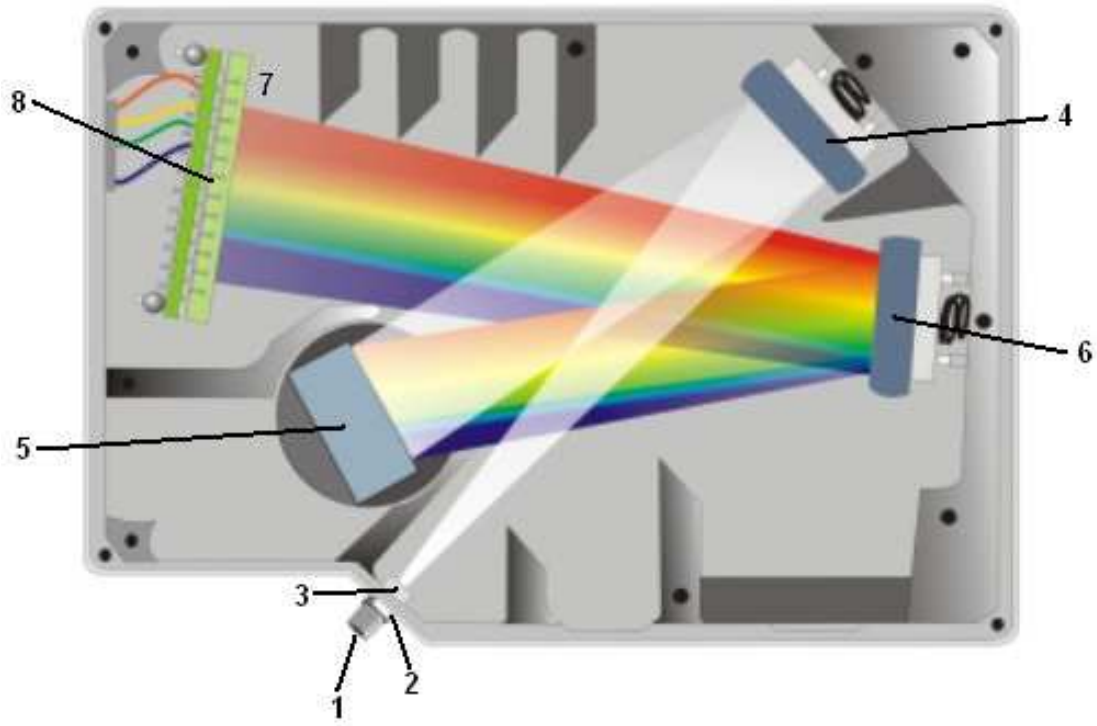

Figure 3.6: The internal workings of the Ocean Optics HR4000 spectrometer. The figure from Ocean Optics HR4000 and HR4000CG-UV-NIR Series High-Resolution Fiber Optic Spectrometers: Installation and Operation Manual. 1) SMA connector 2) Slit 3)Filter 4) Collimating Mirror 5) Grating 6) Focusing Mirror 7) L2 Detector Collection Lens 8) CCD Array

The optical resolution is approximately 1 nm. We established the lower end of the resolution while measuring the sodium doublet of 589.0 nm and 589.6 nm. We did not see a dip between the two peaks of the doublet. Therefore the spectrometer must have a optical resolution greater than 0.6 nm. We then looked at a mercury lamp to see if we could resolve the mercury doublet spacing of approximately 2 nm. We were able to see the separation of the two mercury spectral lines and concluded that the optical resolution has an upper bound of 2 nm.

The input light intensity that the spectrometer measures is rotationally dependent on how the bifurcated fiber optic cable is inserted into the spectrometer. The slit in the spectrometer is not centred on the axes of the fiber optical cable. In figure 3.7, you can see if we rotate the bifurcated fiber optic cable at the connection point you can increase or decrease the amplitude of the light that enters the spectrometer through the 50 micron slit by increasing or decreasing the overlapping area of the fiber and slit. We use this adjustment to set the reflection intensity and transmission intensity to the same signal strength. It is important to keep this in mind when reconnecting the fiber to the HR4000 spectrometer.

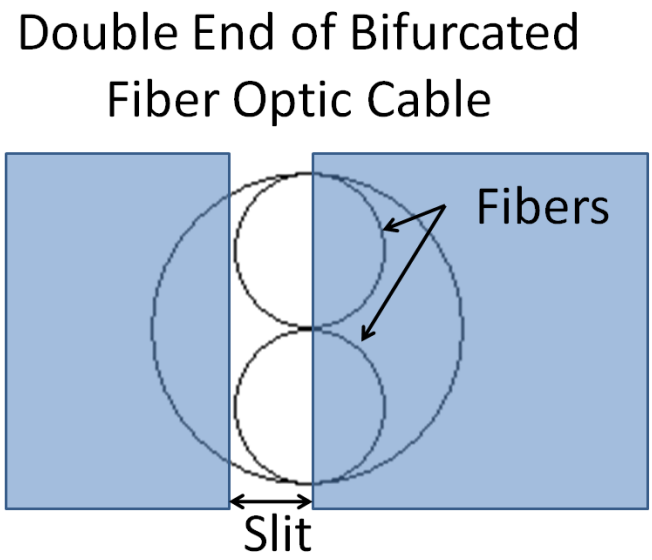

Figure 3.7: The slit of the Ocean Optics spectrometer is offset from the center of the bifurcated fiber optic cable. Rotation of the fiber optic cable will change the intensity of light that enters the spectrometer.

Also, the spectrometer has systematic noise when you set the integration time below 3.8 ms. In Figure 3.8, we can see that the noise starts when the integration time is set to 3.799 ms. The whole spectrum, from 200 nm to 1100 nm, has the noise when we reach 1.350 ms. As we lower the integration time the noise travels from the 200 nm side of the spectrum to 1100 nm side of the spectrum. The lowest recommended integration time would be 3.8 ms due to this systematic noise.

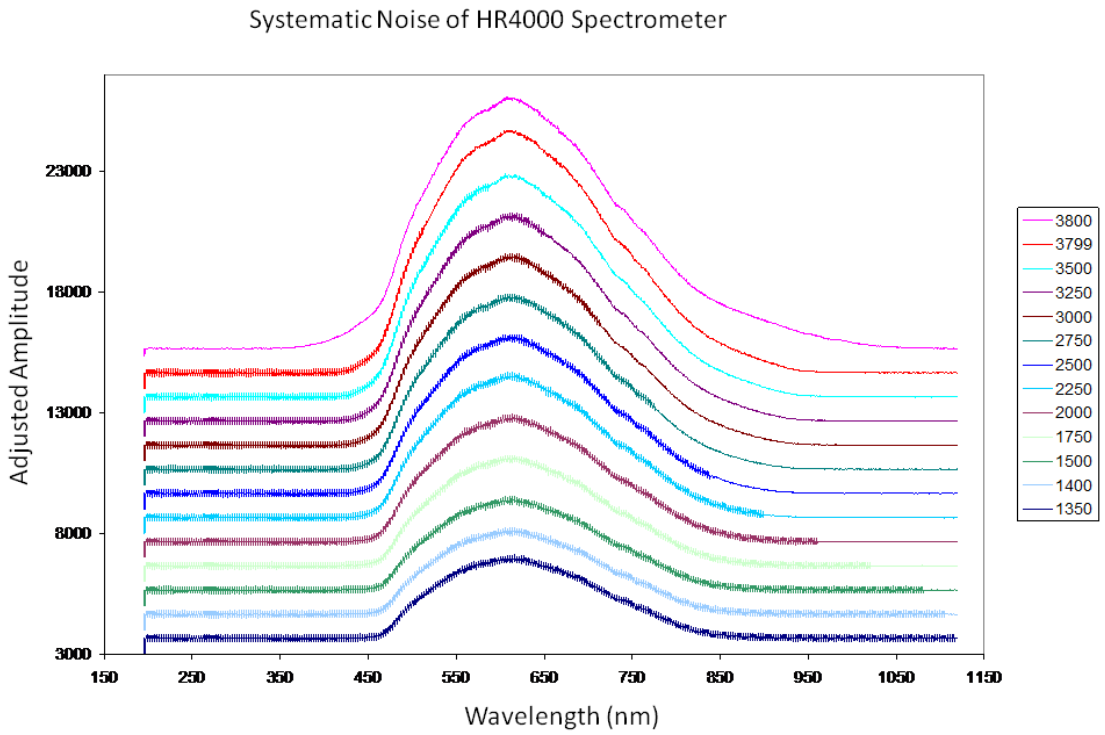

Figure 3.8: The systematic noise of the HR4000 starts when the integration time is set to 3.799 ms and the whole spectrum, from 200 nm to 1100 nm, has the noise when we reach 1.350 ms.

3.1.3.2 NIR256-2.5

The Ocean Optics NIR256-2.5 spectrometer is made up of a Hamamatsu G9208-256 InGaAs linear array detector, SMA connector, 50 μm slit, collimating mirror, and grating [12]. The NIR256-2.5 spectrometer works the same as the HR4000

but without the filters and with a InGaAs detector array instead of the CCD. The input light intensity that the spectrometer measures is rotationally dependent on how the bifurcated fiber optic cable is inserted into the spectrometer as with the HR-4000.

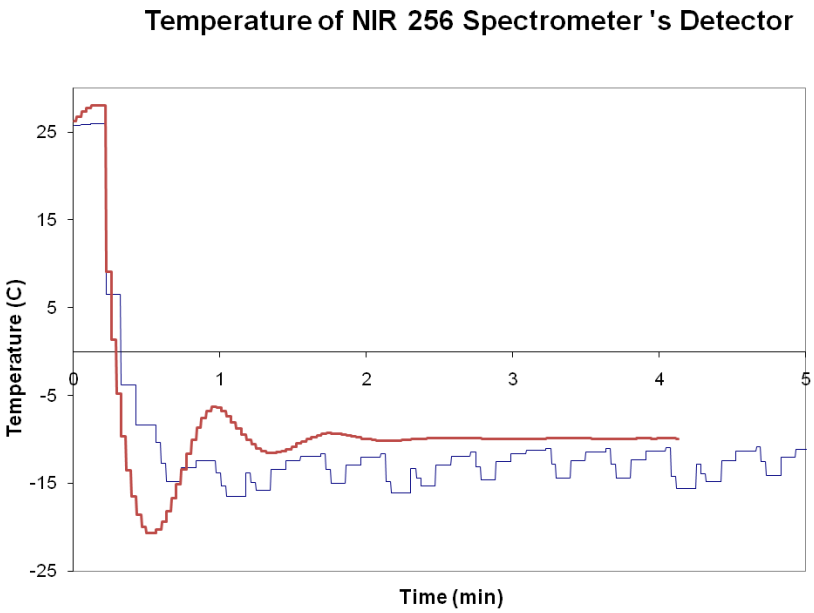

Figure 3.9: The Ocean Optics NIR256-2.5 spectrometer cools in two different modes. The spectrometer will converge to the set temperature with a sinusoidal with an exponential decay envelope or has a step like function where the temperature will vary by 4 degrees during the measurement.

The small band gap of the InGaAs detector requires us to cool the detector to reduce the dark current in the spectrometer. The spectrometer uses thermo-electric cooling with a fan to cool the detector to -10 ^{o}C [12]. When the spectrometer is cooling down to the set temperature it can enter into one of two modes, an

exponentially decaying sin wave or a step function. Both modes are shown in figure 3.9. The exponentially decaying sin wave mode is the mode in which we want to cool the system. The spectrometer cools in a decaying sinusoid fashion until the temperature of the detector is between -10 ^{o}C and -9.9 ^{o}C. The step function mode cools the detector to -15 ^{o}C and then takes steps up to about -11 ^{o}C and then back down to -15 ^{o}C. In the step function mode the temperature varies from -15 ^{o}C to -11 ^{o}C and your measurements will be unreliable because the intensity signal of the spectrometer increases with temperature. The higher the temperature then the larger the intensity signal and noise. The spectrometer will enter one of these two modes at random when starting the program. I have found that if you start the program and it enters the step function mode, then stop the program and disconnect the USB cable from the NIR256-2.5 and then reconnect the USB cable. The spectrometer will now enter the exponentially decaying sin wave mode when you restart the program. In figure 3.10, we show the effect of the cooling of the detector. With the cooling enabled we have a large reduction in the noise on the intensity signal.

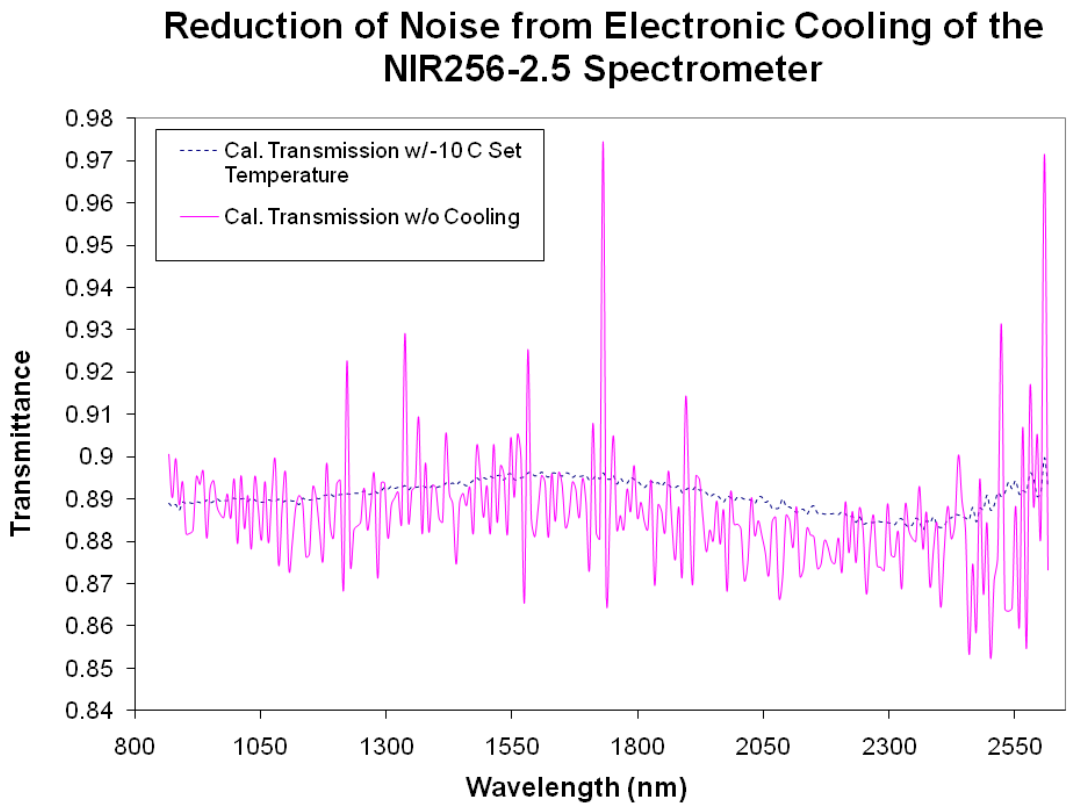

Figure 3.10: The Ocean Optics NIR256-2.5 spectrometer has less noise when cooling option is enabled.

The Ocean Optics NIR256-2.5 spectrometer has a defective pixel, number 56, that is always at the maximum intensity signal. We average out this pixel in the Lab View program by taking the average intensity count from the pixel before, number 55, and the pixel after, number 57.

As you increase the integration time the intensity signal does not increase in a linear fashion. In figure 3.11, we see that some of the intensity signal's amplitudes

increase linearly with integration time while others do not. Starting at an integration time of 10 ms, we measured the lamp spectrum in increments of 10 ms up to 130 ms. We normalize each lamp spectrum to the spectrum of the lamp with an integration time of 5 ms. We looked at every hundredth nanometer wavelength and saw that at low integration times, less than 30 ms, that all the signals behave linearly. With integration times above 30 ms the signals diverge and no longer follow a linear line.

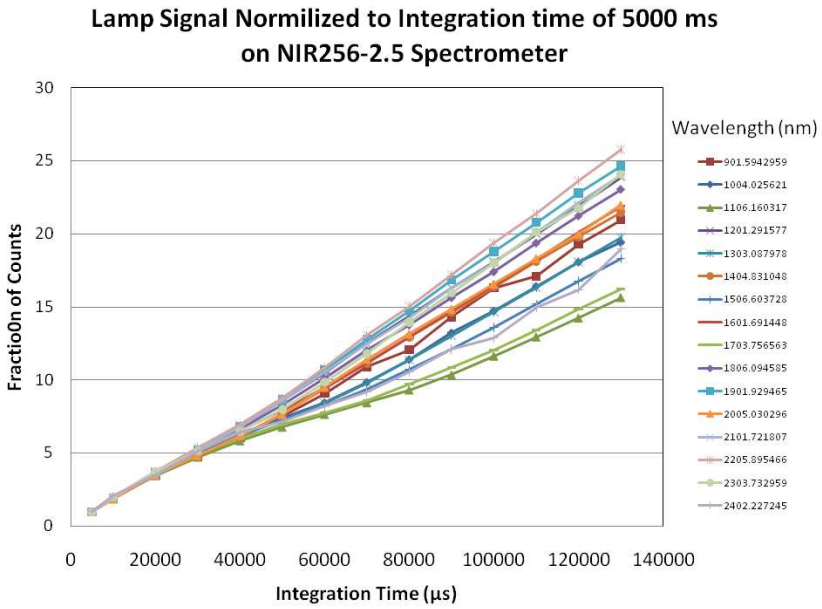

Figure 3.11: The Ocean Optics NIR256-2.5 spectrometer's intensity signals do not increase linearly. After 30 ms the intensity signal no longer increases linearly.

3.1.4 Light Sources

The Fiber Optic Spectrometer uses two light sources to make measurements, the DH-2000-BAL in the ultraviolet-visible part of the spectrum and the HL-2000-FHSA in the near infrared part of the spectrum.

3.1.4.1 DH-2000-BAL

The DH-2000-BAL is used mainly with the HR-4000 spectrometer and is made up of two different lamps, a deuterium lamp and a halogen lamp [13]. In figure 3.12, we see the spectrum of the DH2000-BAL taken with the HR4000 spectrometer. The lamp balances the two lamps with filters and electronic power adjustment to give each lamp approximately the same intensity. To change the relative intensity of the two lamps, adjust the resistor on the back of the lamp housing. The deuterium lamp has a range from 200 nm to 430 nm and the halogen has a range from 430 nm to 2600 nm. Each lamp may be turned on independently.

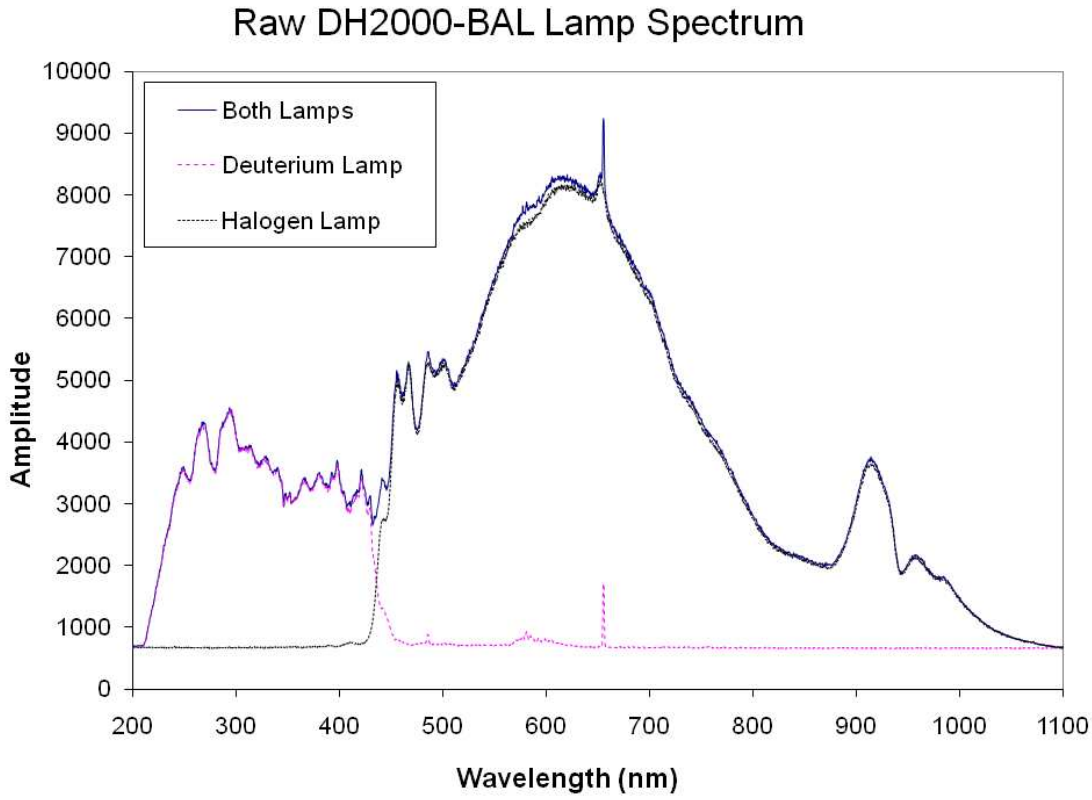

Figure 3.12: The Ocean Optics DH2000-Bal lamp spectrum measured with the Ocean optics HR4000 spectrometer.

At times the lamp has a shift of the halogen intensity by $\pm 10\%$. This shift looks to be sinusoidal with a period of 1 to 2 minutes. The spectrum of the DH-2000-Bal lamp will have a sharp rise or decrease in the spectrum at approximately 450 nm. I believe it has to do with the variable resistor which controls the intensity of the halogen lamp but I am unsure why it oscillates. This happens after the warm up time of 30 minutes and lasted for about a week. After which the lamp then went

back to being a stable source. I have had this experience with the lamp three times in the past two years.

3.1.4.2 HL-2000-FHSA

The HL-2000-FHSA is mainly used with the NIR256-2.5 spectrometer. It is a halogen lamp with a range from 350 nm to 2600 nm. In figure 3.13, we see the spectrum of the HL-2000-FHSA taken with the NIR256-2.5 spectrometer. The warm up time for this lamp is approximately 5 minutes. You can adjust the intensity of the lamp with an attenuation knob on the top of the lamp which lowers a shutter to block the light path way.

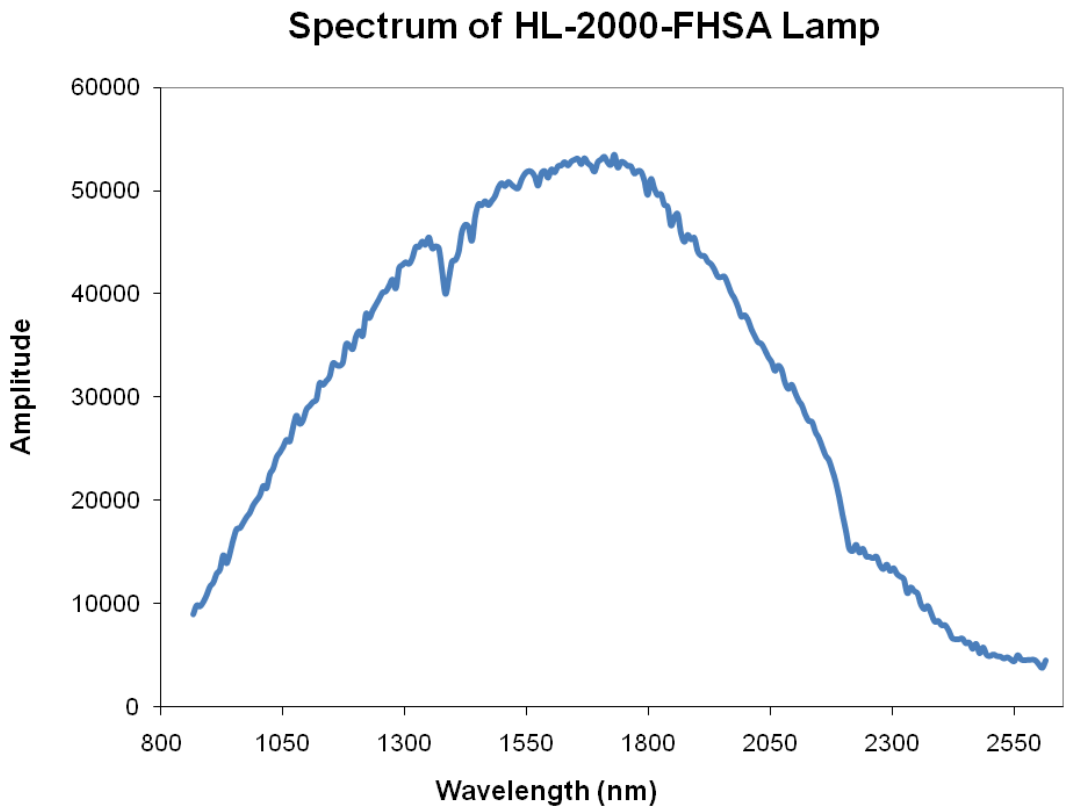

Figure 3.13: The Ocean Optics HL-2000-FHSA lamp spectrum measured with the Ocean optics NIR256-2.5 spectrometer.

3.1.5 Shutter System

The shutter system mechanically opens and closes the light pathways of the fiber optic spectrometer. The shutter system is made up of two main parts: the mechanical components and the electronic components.

3.1.5.1 Mechanical

The mechanical components of the shutter system are made up of four solenoid towers. The solenoids can only pull the shutter. The further the solenoid rod is inside of the solenoid the larger the force the solenoid can pull the shutter with. At the start of each change in shutter position the solenoid does not have enough force to move the shutter. We put a spring on the opposite tower to push the shutter until the solenoid is able to move the shutter. You should hear a click sound when the shutter changes position. There are two solenoids on the transmission cage and two on the reflection cage as shown in figure 3.1.

3.1.5.2 Electrical

The circuit diagram for the shutter system is shown in figure 3.14. We used a DM74LS02N for the NOR gates, BS170 for the transistors, and a Guardian Electric TP8x16 solenoid. We use the breakout box, which is connected to the HR-4000 spectrometer, to send signals to the circuit through ports J2-6 and J2-15. When we send the signal high, about 3.2 V, the NOR gate will return a high signal because the other input is at a constant low signal and turn off the solenoid. When we send the signal low, about 0 V, the NOR gate will return a low signal and turn on the solenoid. The reason for the resistor R1 in figure 3.14 is to pull down the signal to 0 V when the program sends a low signal. Without the resistor, the lowest the breakout box output voltage can go is 1.6 V. R2 is there to provide the correct amount of current to the gate. We want a 10 to 1 ratio between the current that

goes through the sink and gate. We have about 250 mA going through the sink and about 21.5 mA going into the sink. The diode is critical to make sure that the transistors do not burn out while turning on and off the solenoids. The most current we can send into the breakout box is 10 mA and when we send the low signal we send the most current, approximately 7.5 mA, into the breakout box.

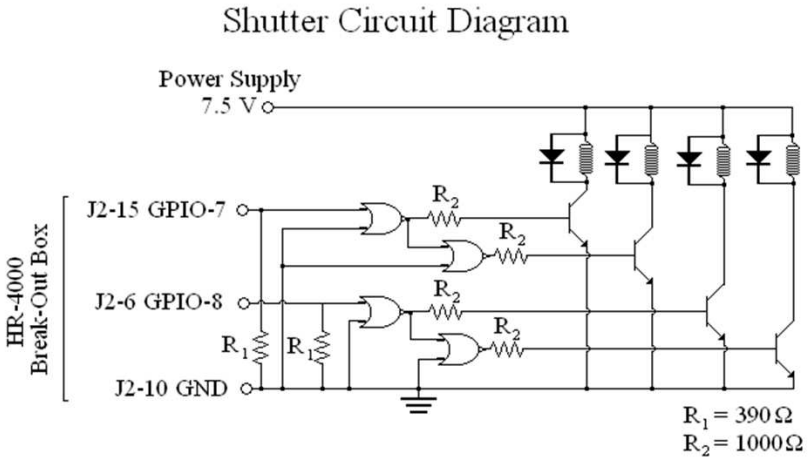

Figure 3.14: The shutter control circuit.

3.1.6 Optical Cages

There is a reflection and transmission cage for the HR-4000 spectrometer and a reflection and transmission cage for the NIR256-2.5 spectrometer. The sample is placed in the transmission cage for each spectrometer while performing a measure-

ment.

The transmission cage is made of two xy translational stages, two fiber optic collimating lenses, two focusing lenses, and a shutter. In figure 3.15, we see the arrangement of the transmission cage. You can adjust the light path several ways with this cage. First the xy translation stage moves the fiber in the xy plane. Next you can slide the fiber optic cable in and out of the fiber optic collimating lens. This will cause the light beam to become more or less collimated. For a collimated beam you will need to pull the slide out 7 mm from the fully inserted position. You can also adjust the position of the focusing lenses by screwing them in and out of the optical blocks. Finally, you can rotate the lamp fiber optic cable in the fiber optic collimating lens. The fiber in the lamp end of the transmission cage is a bifurcated cable. Rotating the cable will increase and decrease the intensity of light that enters into the reflection cable.

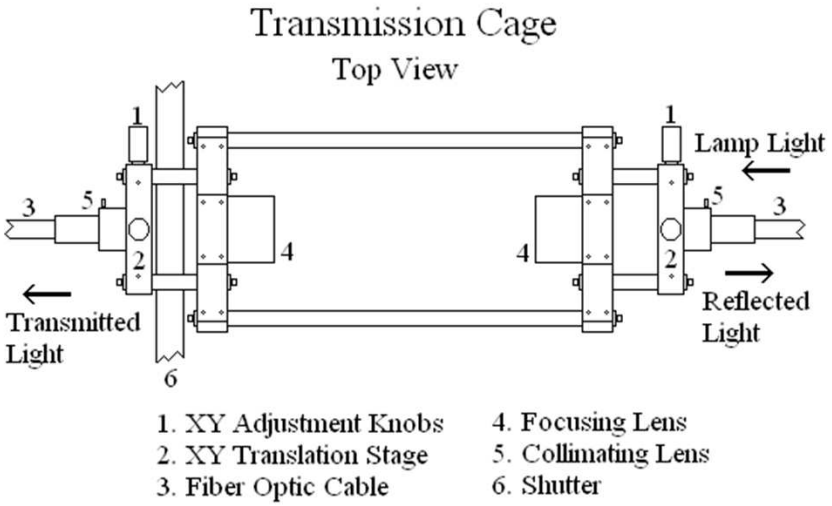

Figure 3.15: The transmission cage on the Ocean Optics spectrometer.

When we take a transmission measurement, the light from the lamp follows the path shown in figure 3.3. The lamp light comes out of the fiber optic cable and then goes through a collimating lens. Then the light travels through a focusing lens which focuses the lamp light to a spot that is about 1 mm in diameter. The light then travels through the sample and is collimated with a second focusing lens. The light is coupled into the fiber optic cable with a second collimating lens.

We found that the measurements are more consistent if we adjust the lamp collimating lens to the fully inserted position. This does not allow the light to be collimated as it leaves the collimating lens. This causes the amplitude of the transmitted light to decrease but causes a more stable intensity signal. I believe this is because of small vibrations of the optical table which cause the light to

shift side to side when coupled into the fiber optic cable. If the vibration shifts the light path to the side during a sample measurement then you will get less light in the fiber optic cable than you did with the reference measurement. This will cause a decrease in the fraction of the transmission values, lowering the measured transmittance of the sample. If we make the spot size larger or smaller, the effect of the vibrations is decreased. Figure 3.16 shows how the larger and smaller sized spots lessen this problem.

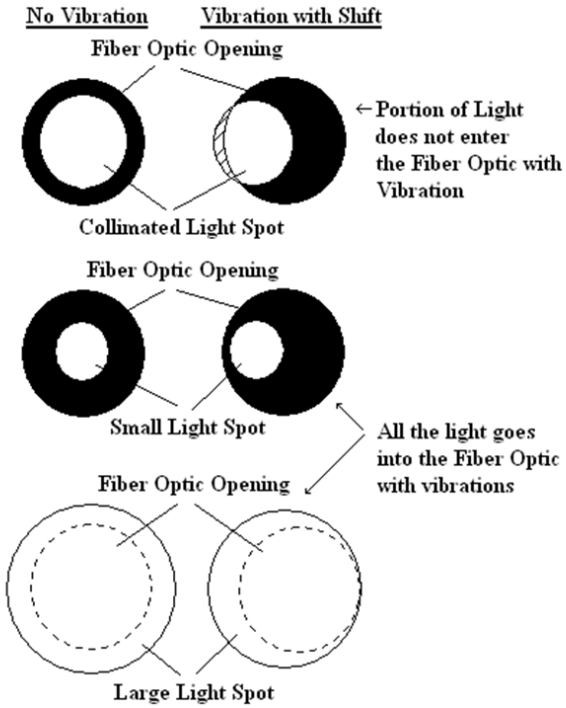

Figure 3.16: The spot size on the transmission cage spectrometer fiber optic needs to be defocused so that you will not get a variation in the signal caused by vibrations of the optical table.

With the fiber optic cable positioned so the light beam is collimated then we can get $\pm 5\%$ variation in our transmission spectrum. When we positioned the fiber optic cable in the fully inserted position, the spectrum shifts are greatly reduced.

The reflection cage is made of xy translational stages, an angular stage, two fiber optic collimating lens, and a shutter. In figure 3.17, we see the arrangement of the reflection cage. The purpose of the reflection cage is to allow us to turn on and off the reflected light from entering into the spectrometer. We align the cage such that the light will pass through with minimal intensity loss.

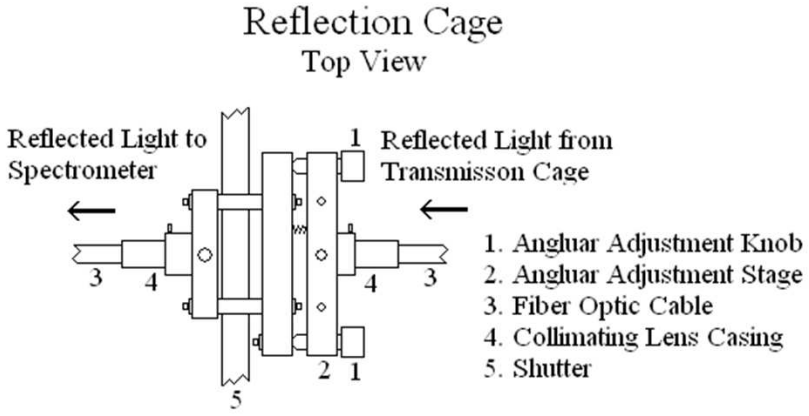

Figure 3.17: The reflection cage on the Ocean Optics spectrometer.

When taking reflection measurements we have noticed a chromatic aberration from the focusing lenses. In figure 3.18, we moved the reflective standard along the z axis of the transmission stage and took a spectrum at each position. We can

see a peak move from low wavelength to high wavelength as the mirror is moved further from the focusing lens.

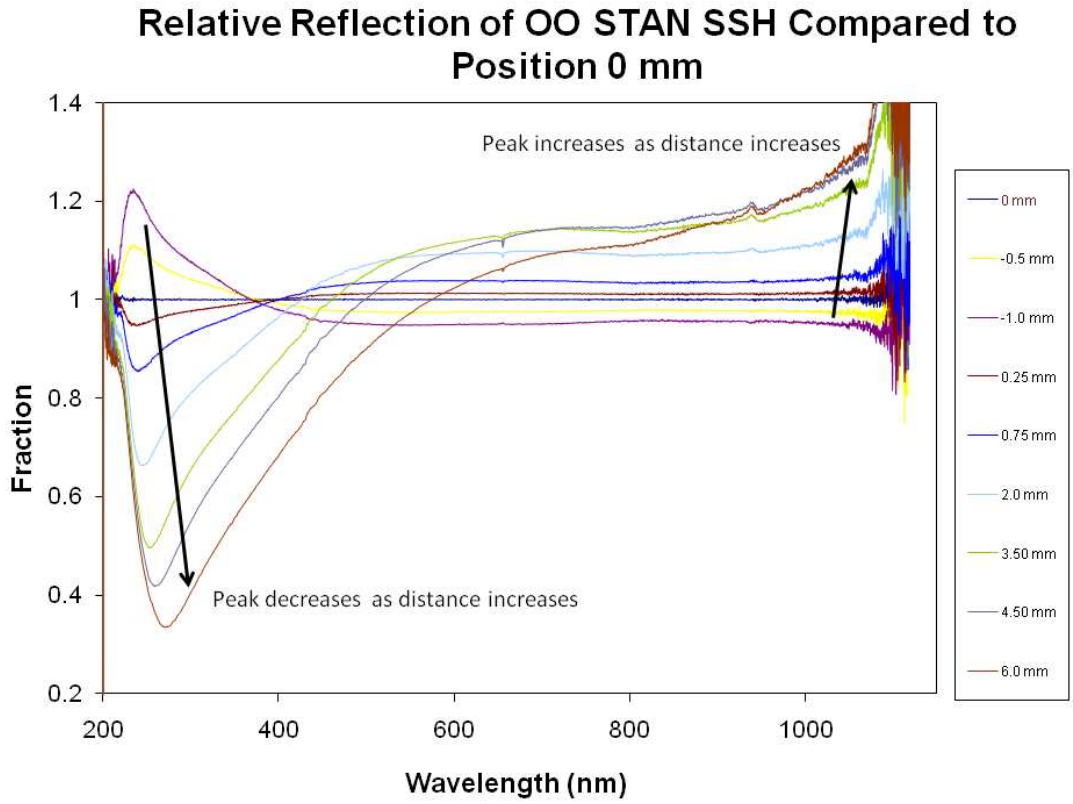

Figure 3.18: The peak of the reflection is dependent on the position in the optical cage. The closer the sample is to the lamp fiber optic then the higher the ultraviolet region will be. The infrared region will increase when the sample is further away from the lamp fiber optic.

3.1.7 OO STAN-SSH Reflection Standard

The reflection spectrum of the OO STAN-SSH reflection standard is shown in figure 3.19. We can see a sharp drop off from 200 nm to approximately 300 nm. We also see a minimum at 850 nm. The reflectivity spectrum shown in figure 3.19 is stored in the spectrometer's Lab View program and is used as the reflectivity reference any time we make a reflective measurement.

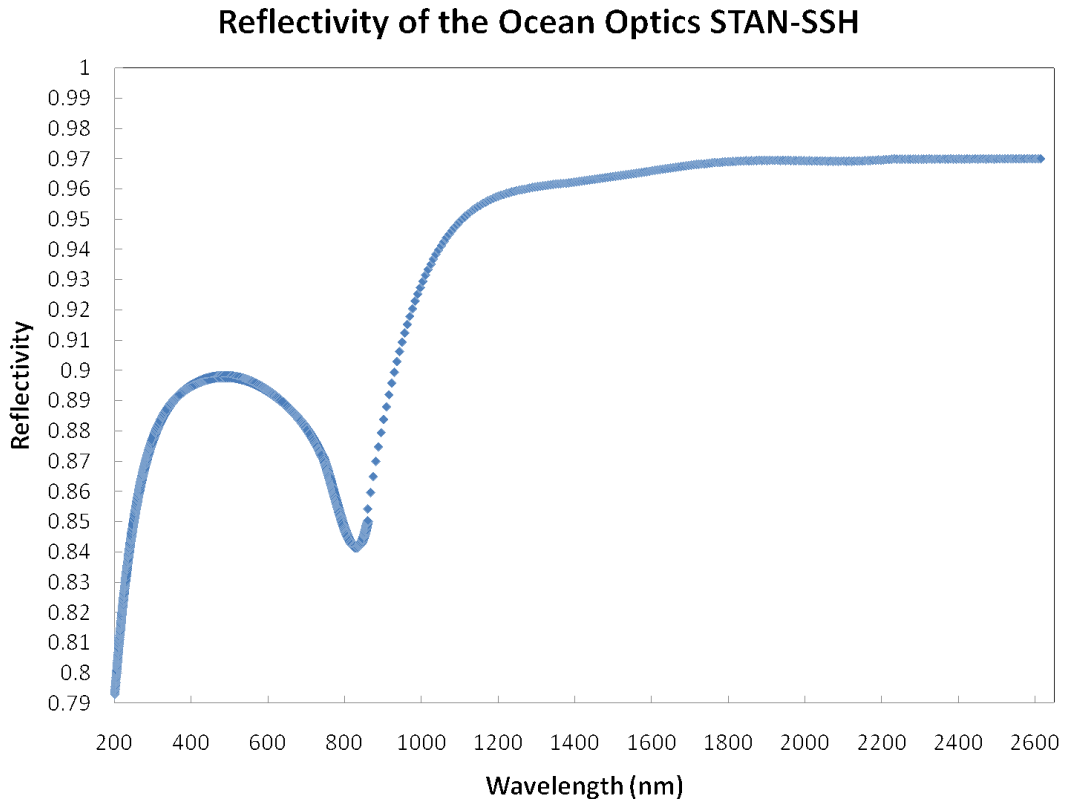

Figure 3.19: The reflection spectrum of the Ocean Optics STAN-SSH reflection standard measured with the scanning monochromator with the ultraviolet region fitted to the Ocean Optics reflection spectrum and adjusted to a line with the scanning monochromator data.

The Ocean Optics STAN-SSH is an aluminium reflection standard mirror and the main standard for the fiber optic spectrometer. We tested the uniformity of the reflection standard as shown in figure 3.20. We scanned the surface of the mirror in 2 mm steps taking a reflection spectrum at each location. We found the

reflectivity of all wavelengths to be within 0.01% of each position. The spikes on the edges of the plot in figure 3.20 are caused from the light reflecting off the edge of the mirror.

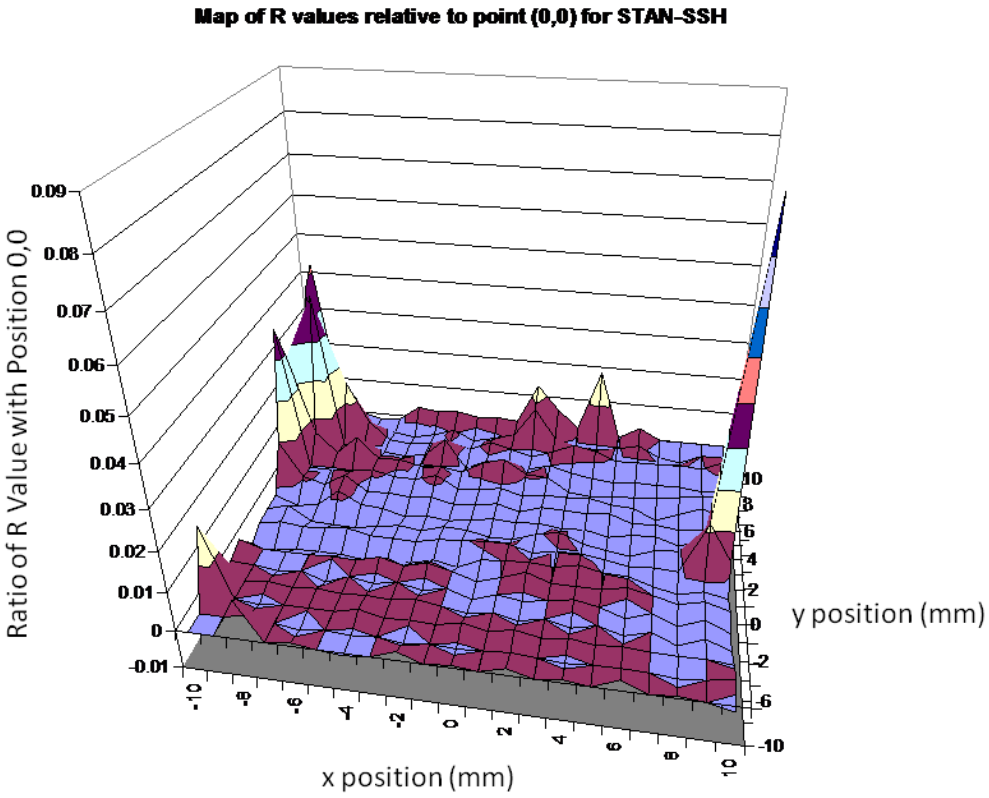

Figure 3.20: The map of the surface of the Ocean Optics STAN-SSH reflection standard. We can see that the reflectivity does not change more than the 0.01 percent over the surface of the mirror. The peaks are from the light striking the edge of the mirror.

3.2 Scanning Monochromator

We measure the diffuse reflection of a sample by shining broadband light on the powder material and collecting light which reflects off of the sample. With the scanning monochromator we use an integrating sphere to collect the diffusely reflected light off of the sample.

The scanning monochromator has Oriel 7340 Xe and W lamps powered by a Schoeffel LPS 251 lamp power supply. It uses a Thor Labs SM1PD1A Si detector and a Thor Labs SM05PD5A InGaAs solid state detector. The light from the lamp first goes through a double Oriel 77276 monochromator which uses a 2, 1, 0.5, or 0.25 micron grating depending on which wavelength range you are measuring. The monochromator separates the lamp light into different wavelengths. The light then goes through a filter to block the second and third order reflections off of the grating and is steered to the top of the Oriel 70491 integrating sphere with aluminium mirrors. The powder samples were placed at the bottom of the integrating sphere. This geometry will allow for any specular reflection to escape out the top of the integrating sphere. The detector is located at 90 degrees to the sample and the lamp light entrance port. The detector converts light intensity into a current signal which is then read with a Newport 835 optical power meter.

When taking a diffuse reflection measurement we mount the sample in an 2.25 mm deep ceramic dish. We compact the sample with a glass slide to give an approximately flat surface. We place a piece of black paper which is angled at approximately 45 degrees from the lamp light and record a background spectrum.

Next we place the diffuse reflection standard in the sample port and record the reference spectrum. We assume that the reflection standard is 100 percent reflective. In the measurements reported here we used a $BaSO_4$ reflection standard, which is the same material that is deposited on the inside of the integrating sphere. Now we insert the powder sample into the sample port of the integrating sphere. We then take the sample spectrum and the spectrometer's Lab View program averages a chosen number of spectra and then calculates the diffuse reflection spectrum with equation 2.4.

Chapter 4 – Bifurcated Fiber Method for Measurement of Bandgap Energy

The diffuse reflection of a material is very much like the transmission spectra. We see an onset of the absorption around the location of the bandgap of the material. To find the bandgap energy of a material we start with the measured diffuse reflection. In figure 4.1, we see a diffuse reflectance spectra of TiO_2. The bandgap onset is clearly seen at about 350 nm.

The bandgap energy of powder material is found by calculating the absorption spectrum from the diffuse reflection spectrum. We use Kubelka Munk theory to calculate the ratio of absorption coefficient and scattering coefficient, as shown in equation 2.27. Here we assume that the scattering coefficient is constant over the wavelength region that we are measuring.

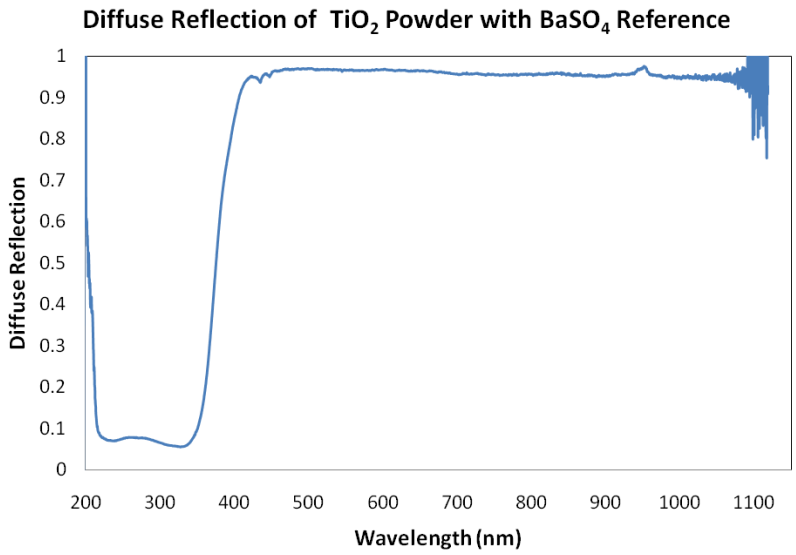

Figure 4.1: The diffuse reflectivity of TiO_2 powder. We can clearly see the bandgap onset at about 350 nm.

4.1 Bandgap Energy Calculations

When calculating the bandgap energy of a powder material, we need to look at the diffuse reflection spectrum for the bend or onset of the bandgap. We also look at the absorption spectrum for where the linear fit to the bandgap onset crosses the baseline absorption to find the bandgap energy. The baseline absorption will be defined by the region of the spectrum at lower energy than the bandgap. In most cases the baseline absorption will be on or slightly above the energy axis but, in the infrared region of the spectrum we start to see the effects of scattering and

the baseline absorption could be above the energy axis. In figure 4.2, we see the absorption spectrum calculated using equation 2.27 from the reflection spectrum in figure 4.1.

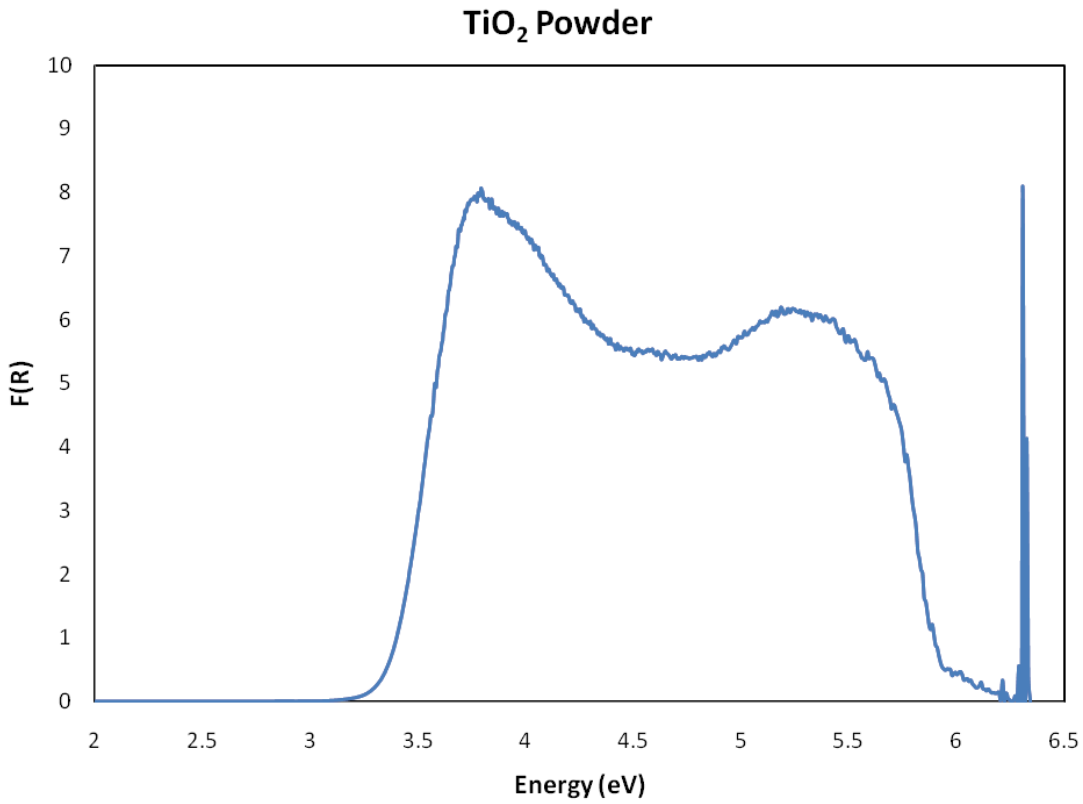

Figure 4.2: The absorption spectrum of TiO_2 powder. We assume that the scattering coefficient is constant over this wavelength region.

Now we plot $(F(R)\omega\hbar)^{\frac{1}{2}}$ against $\omega\hbar$ and fit the linear part of the spectrum at the onset to find the bandgap energy. In figure 4.3, we believe the baseline absorption is nearly zero or just above the energy axis.

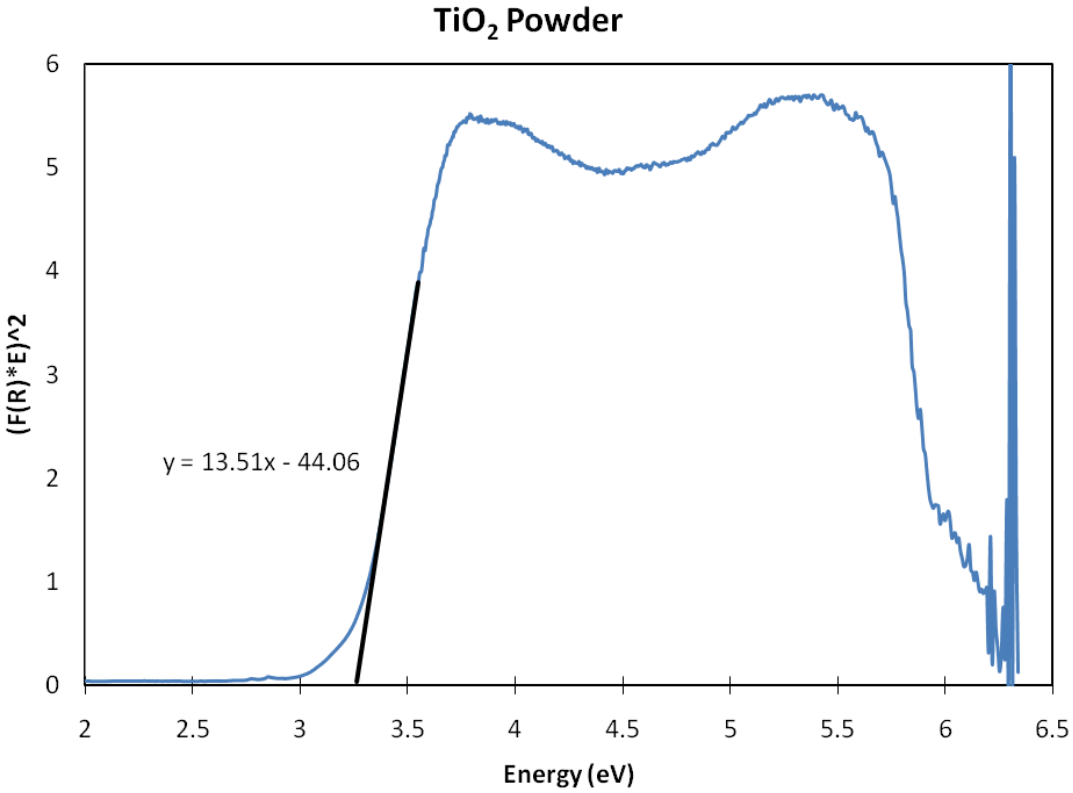

Figure 4.3: The bandgap energy of TiO_2 powder is found by plotting $(F(R)\omega\hbar)^{\frac{1}{2}}$ against $\omega\hbar$ and fitting the linear part of the spectrum at the onset.

The bandgap energy is calculated to be 3.26 eV for the TiO_2 powder.

Now we will look at a powder material in the infrared region of the spectrum. In figure 4.4, we see the diffuse reflection of Sn_2S_2 powder. The bandgap onset falls in the overlap region of the two spectrometers. We can see that the region above the bandgap onset is not flat as it was with the TiO_2 powder but has a positive slope to it.

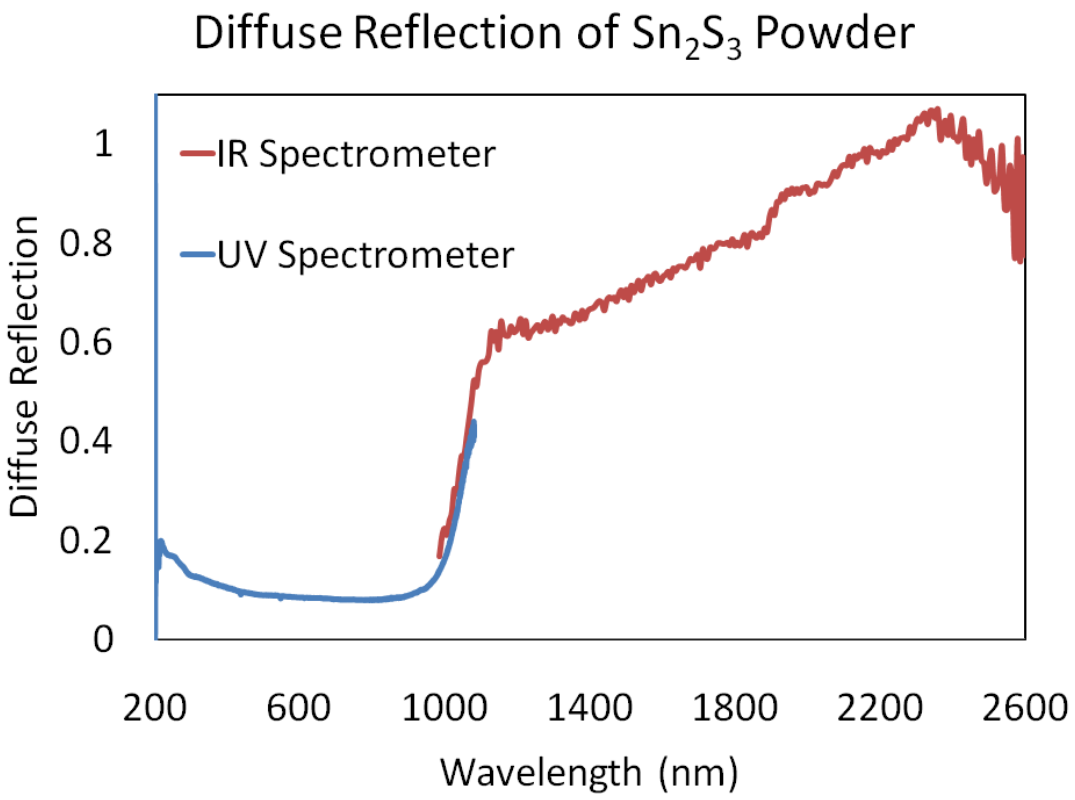

Figure 4.4: The diffuse reflectance of Sn_2S_3 powder.

Now we plot $(F(R)\omega\hbar)^{\frac{1}{2}}$ against $\omega\hbar$ and fit the linear part of the spectrum at the onset to find the bandgap energy. In figure 4.5, we see that the baseline absorption is fitted as well as the bandgap linear region. If we were to extend the bandgap fit to the energy axis then we would have a bandgap just below 1.1 eV. We see by fitting the baseline absorption we get a bandgap energy of 1.14 eV which is much closer to the Sn_2S_3 thin film bandgap energy of 1.16 eV [14].

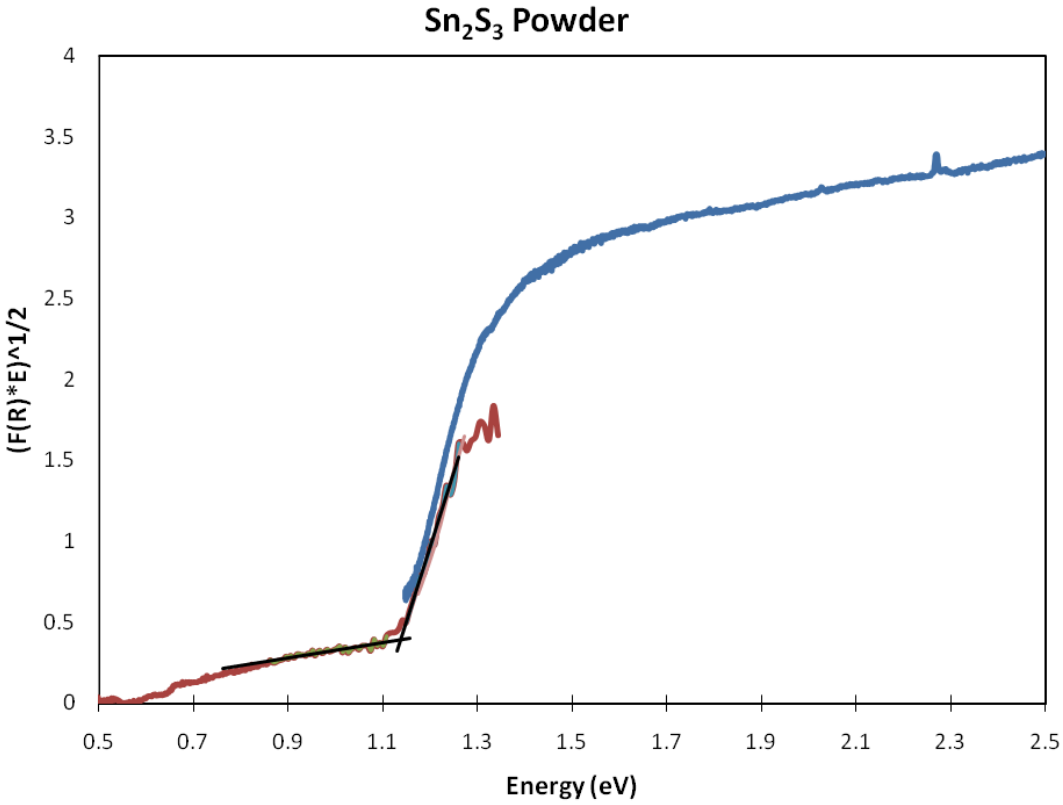

Figure 4.5: The bandgap energy of Sn_2S_3 powder is found by plotting $(F(R)\omega\hbar)^{\frac{1}{2}}$ against $\omega\hbar$ and fitting the linear part of the spectrum at the onset.

4.2 Bandgap Comparison

We first compare the diffuse reflection spectrum of powder samples measured with both the bifurcated fiber method and the integrating sphere method. We can see the two spectra for TiO_2 in figure 4.6. We see that we get the same structure with both spectra. The Ocean Optics diffuse reflection spectrum is cleaner than the

grating spectrometer's diffuse reflection spectrum in the ultraviolet region of the spectrum.

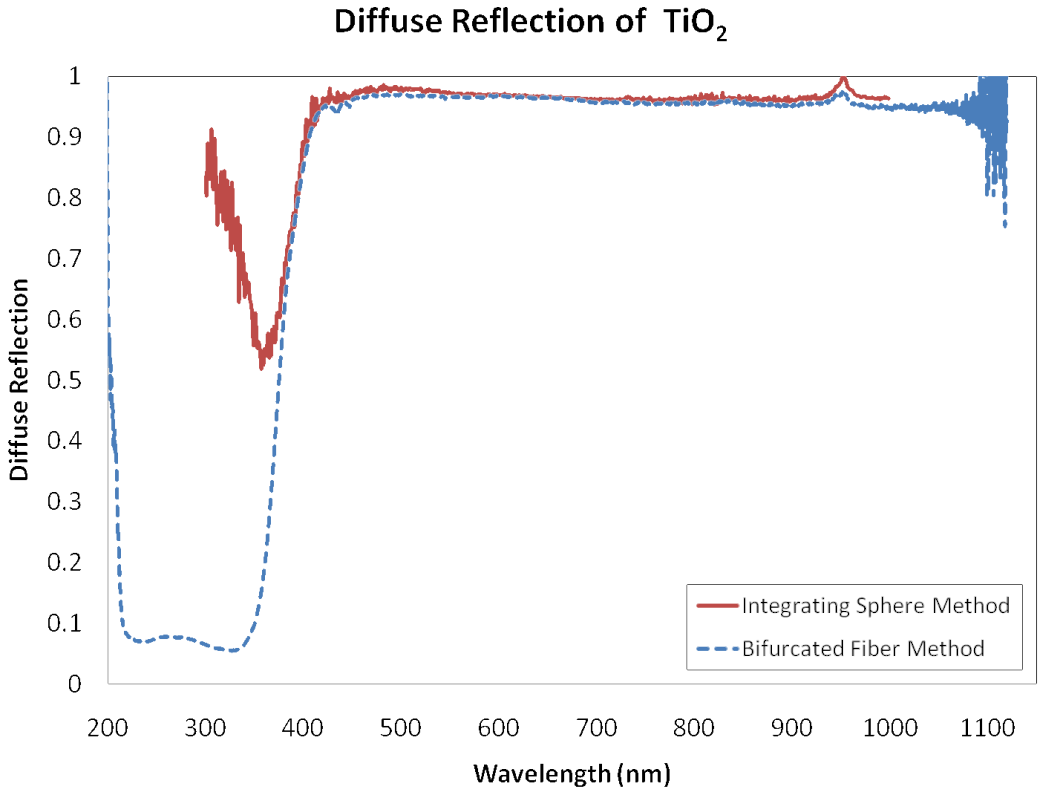

Figure 4.6: The diffuse reflectance of TiO_2 measured with the bifurcated fiber method and the integrating sphere method. We can see that they are basically the same.

Now looking at the infrared region of the spectrum we see the diffuse reflection spectrum of Sn_2S_3 powder measured with both methods in figure 4.7. We get the same structure with both spectra. The Ocean Optics diffuse reflection spectrum is

noisier than the grating spectrometer's diffuse reflection spectrum in the infrared region of the spectrum.

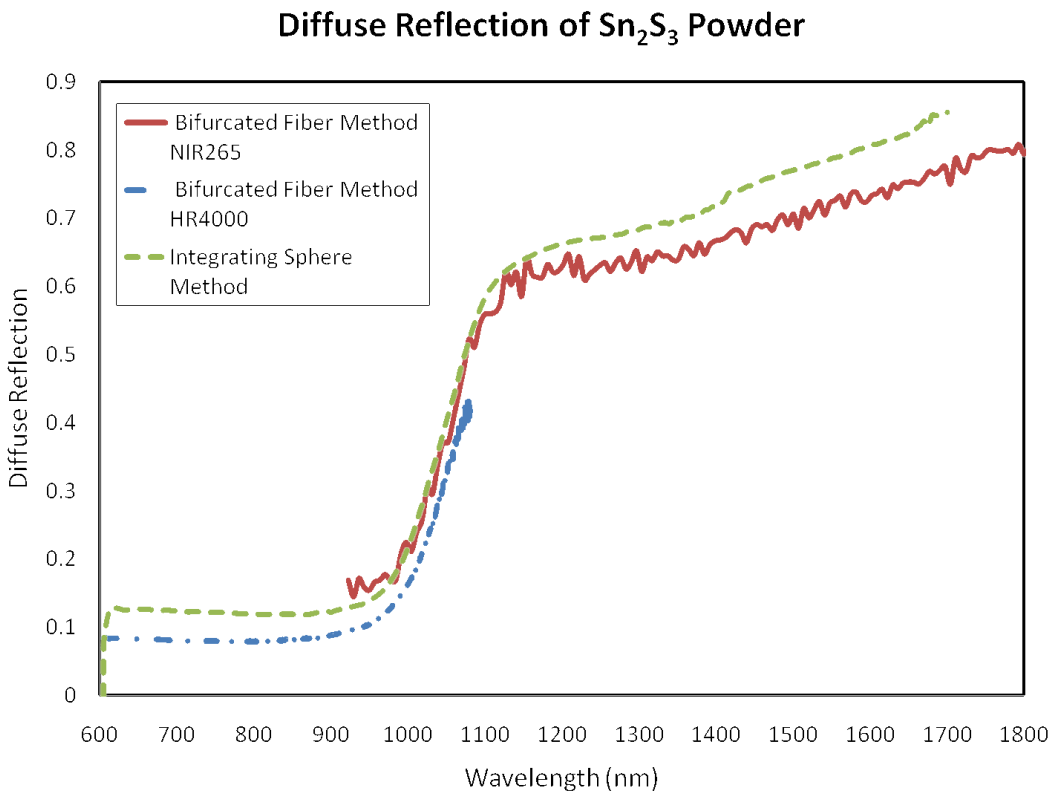

Figure 4.7: The diffuse reflectance of Sn_2S_3 measured with the bifurcated fiber method and the integrating sphere method. We can see that they are basically the same.

We measured the bandgap energy of several powder samples with the Ocean Optic spectrometer using the bifurcated fiber optic method and the scanning monochromator using the integrating sphere method. In figure 4.8, we compare

the bandgap energies of the different powders measured with both methods which agree within 0.03 eV.

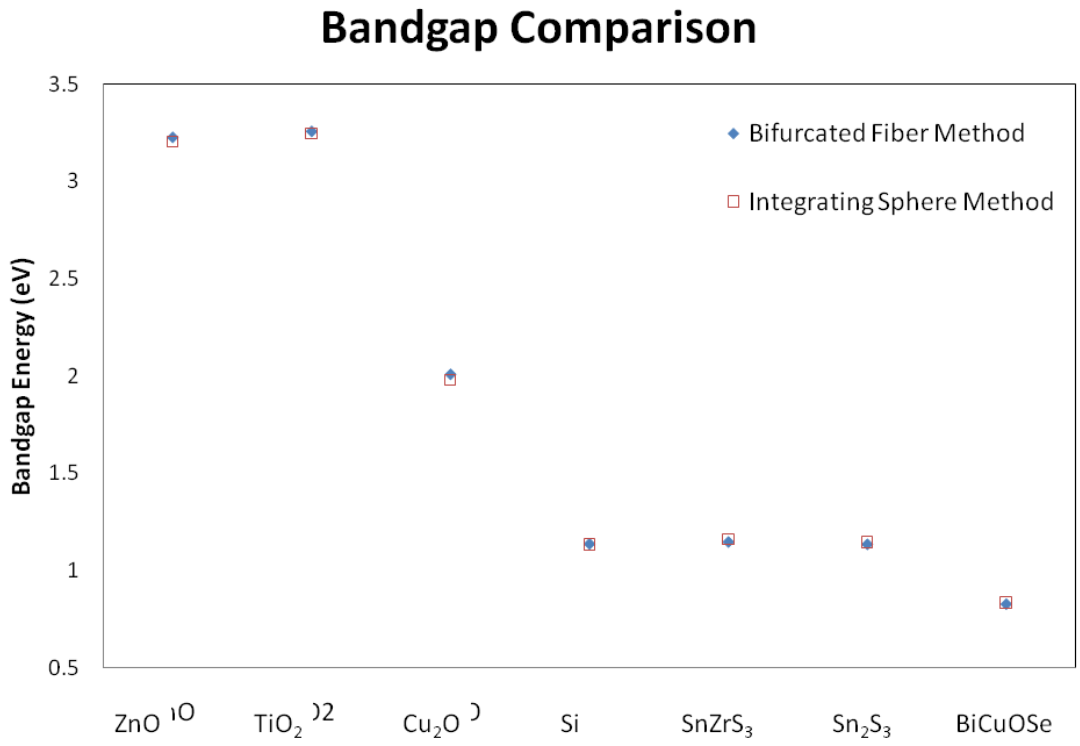

Figure 4.8: Bandgap energies of 7 powdered samples taken with the bifurcated fiber optic method and the integrating sphere method.

Powder Sample	Bifurcated Fiber E_{BG} (eV)	Integrating Sphere E_{BG} (eV)	ΔE_{BG} (eV)
ZnO	3.23	3.21	0.02
TiO_2	3.26	3.25	0.01
Cu_2O	2.01	1.98	0.03
Si	1.14	1.14	0.01
$SnZrS_3$	1.15	1.16	-0.01
Sn_2S_3	1.14	1.15	-0.01
BiCuOSe	0.83	0.84	-0.01

4.3 Scattering Problem

We would expect the region of the spectrum above the bandgap onset in a wavelength *vs* diffuse reflection plot, what we call the baseline absorption, to be constant as a function of wavelength. Instead we see in most of our infrared spectra the baseline absorption has a positive slope to it. Above the bandgap onset the absorption should go to 0 and the only structure should be caused by the scattering coefficient as shown in equation 2.27. We investigated the cause of the positive slope by looking at Si powder and Si single crystals. We took a transmission and diffuse reflection spectra of a Si single crystal with the surface cut on the 1, 1, 1 plane. We used a Perkin Elmer LAMBDA 950 spectrometer with an 150 mm integrating sphere attachment. The transmission spectrum includes all transmitted

light at the position $x = 0$, or $I(0)$, in figure 2.4. We can see in figure 4.9 that the transmission spectrum's baseline absorption is flat with no or a very small slope. The diffuse reflectance of the Si single crystal shows a positive slope for the baseline absorption. The diffuse reflection spectrum includes only the diffusely reflected light. The secularly reflected light exited the integrating sphere through the lamp entrance port. We suspected that if the baseline absorption slope comes from scattering events in the material then we should see a slope in the baseline absorption of the transmission spectrum. If the particle size is below 85 microns, then Ciurczak claims that the particle size will greatly reduce the particle size effects on the scattering coefficient in the near infrared region of the spectrum [15].

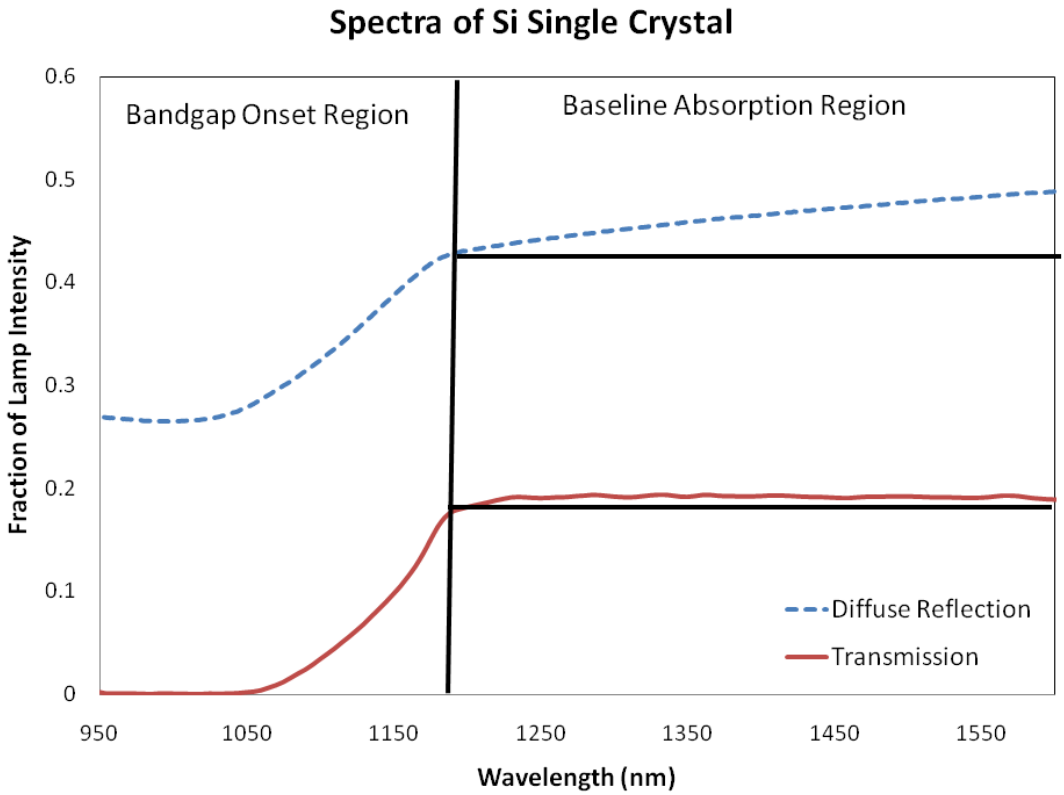

Figure 4.9: Diffuse reflection and transmission spectra of Si powder. Both the transmission and diffuse reflection spectra were measured with an integrating sphere.

We then considered the size of the powder particles. In figure 4.10, we see the Si powder particles. We estimated the size of the powder particles from optical observation to be between 1 micron and 10 microns. The size of the Si particles are typical of all powders in this comparison.

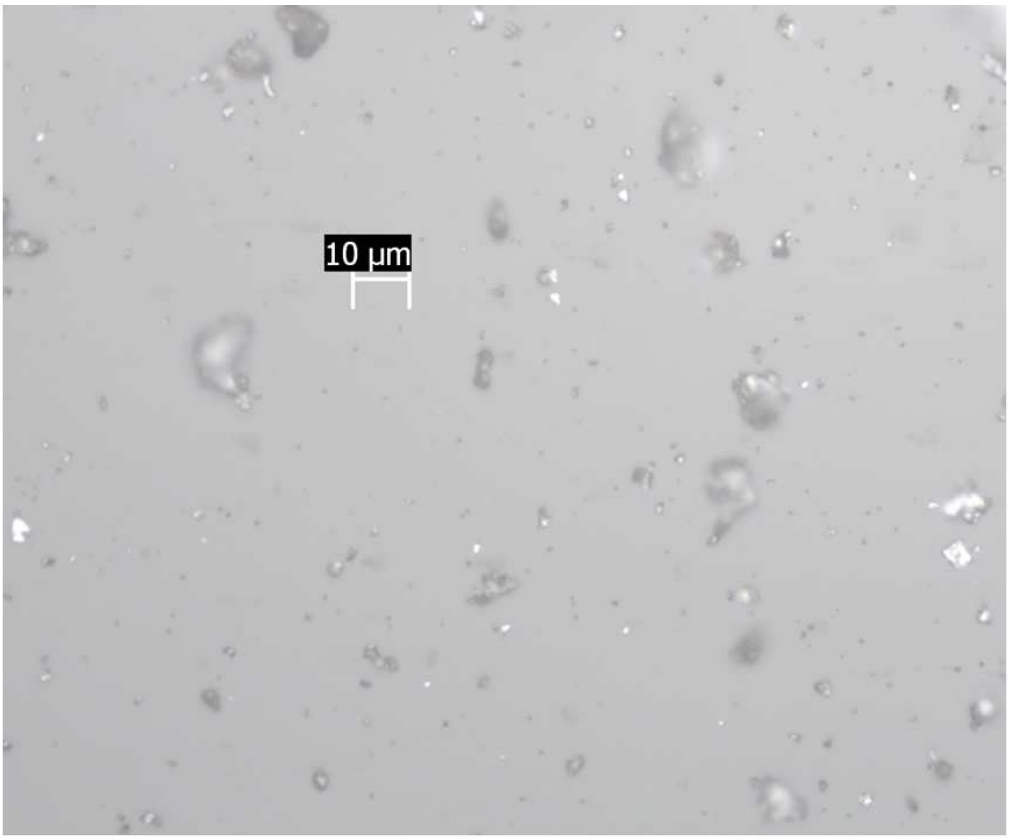

Figure 4.10: Si powder viewed under 100 times magnification. The powder particles range from 1 micron to 10 micron sizes.

We took a diffuse reflection spectrum of the Si powder before and after grinding the powder in a stone crucible. We also ground the powder a second time but did not see much of a change in the baseline absorption slope. In figure 4.11, we see that for the non ground powder the slope is smaller than the two ground powder's slopes. This suggest that the smaller the powder the steeper the baseline absorption slope will be.

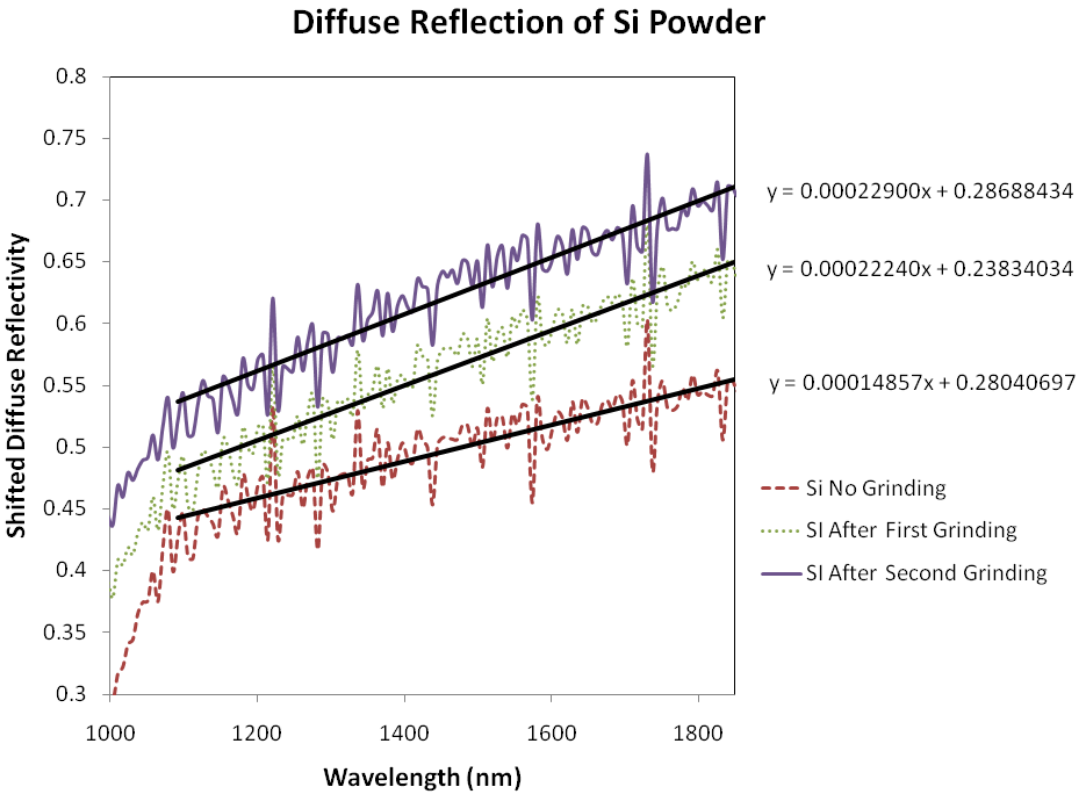

Figure 4.11: The diffuse reflection of Si powder before and after being ground in a stone crucible. We see that the smaller the particle size the steeper the baseline absorption slope.

Next we considered the thickness of the powder sample as the cause of the slope of the baseline absorption. The reasoning was that if some of the light is being reflected off of the ceramic cup holding the powder then the wavelength dependence could come from different penetration depths of the wavelengths. We measured the diffuse reflectance of Si powder with the powder thickness ranging

from 0.32 mm to 2.25 mm. In figure 4.12, we see that the baseline absorption slope does not change as we change the thickness.

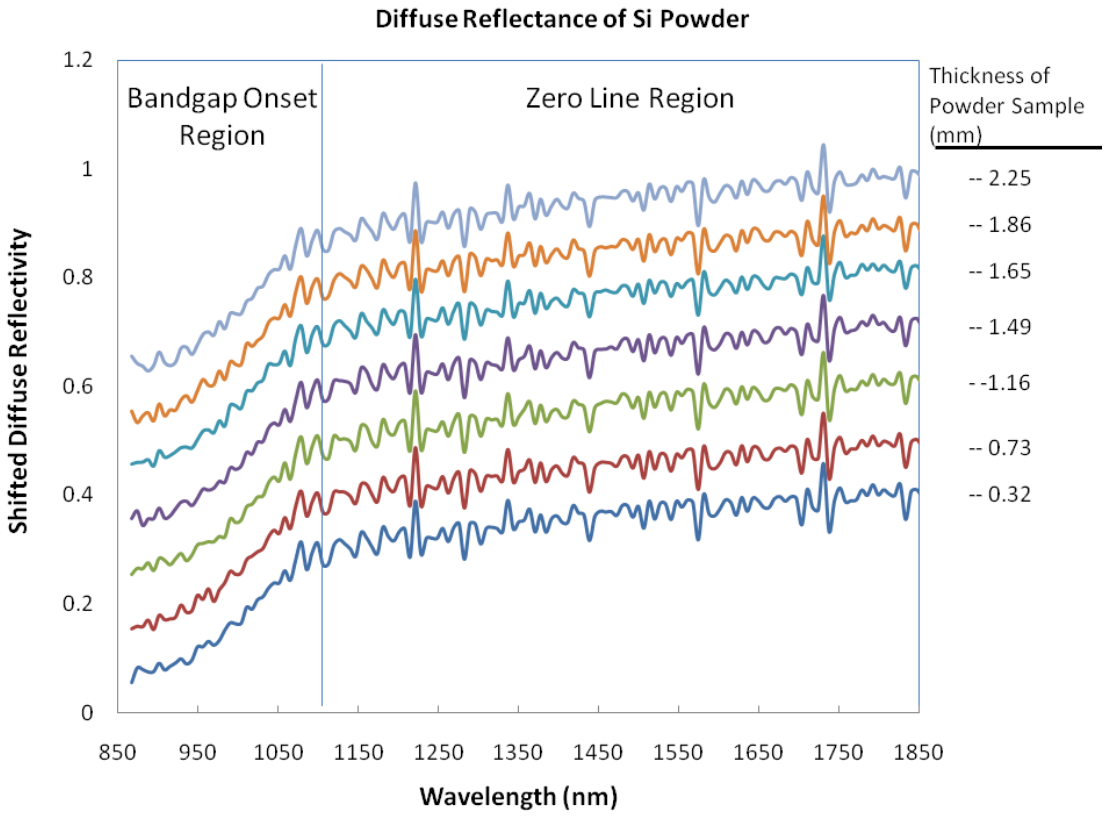

Figure 4.12: Diffuse reflection of Si powder with the powder thickness ranging from 0.32 mm to 2.25 mm. We see no change in the baseline absorption slope as the thickness changes.

We also considered the surface roughness of the Si single crystal. We took a single crystal and polished it with 80 grit, 500 grit and 1 micron sized diamond polish. We took the diffuse reflectance of each roughness and found that an increase

of roughness increases the baseline absorption slope. This single crystal had a negative baseline absorption slope which is not what we see with powder samples. We suggest that the rougher the surface the more specular reflection reflects at a non normal angle. The additional specular reflection appears in the measurement as additional diffuse reflection. The roughness peaks depth range from 1 to 2 nm for the diamond polish to 1 to 2 microns for the 80 grit sand paper.

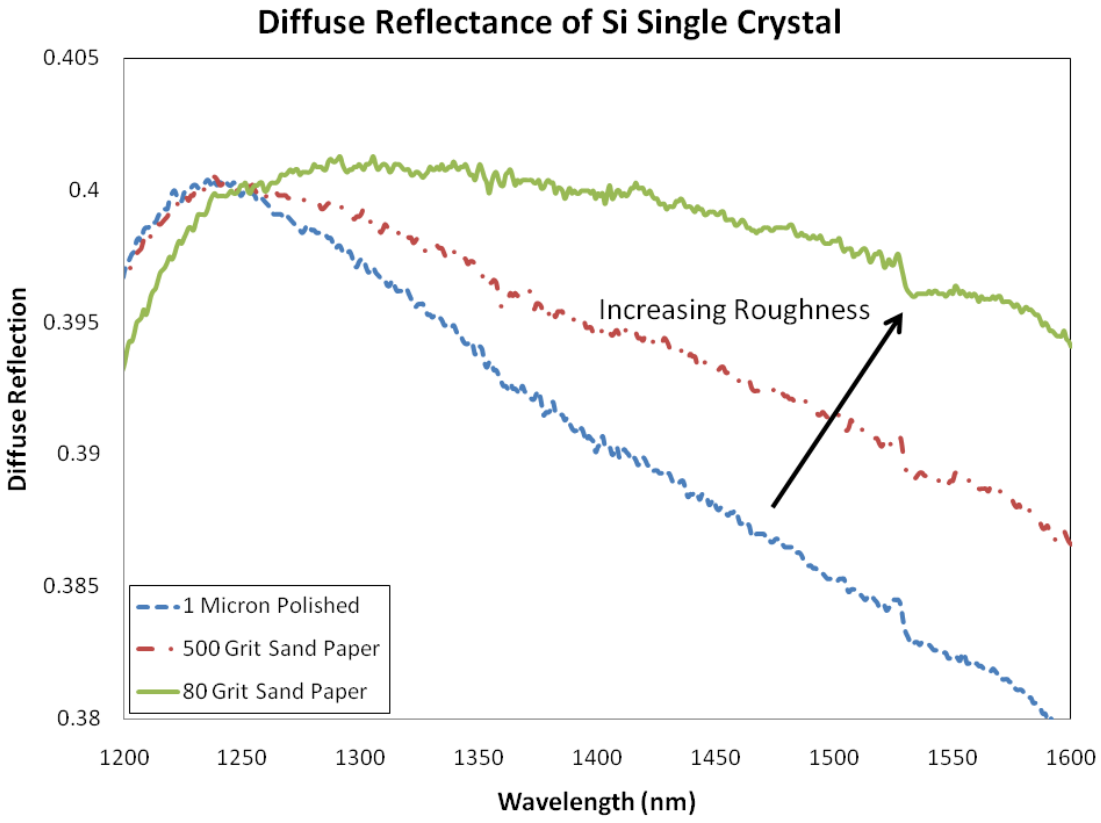

Figure 4.13: Diffuse reflection of Si crystal with the different surface roughness. We see an increase in the baseline absorption slope as the roughness increases.

The scattering of the powder material is complex and depends on the particle size and the surface roughness. The baseline absorption scattering problem needs further research and explanation.

4.4 Optical Bowing

While making the comparison between the bifurcated fiber method and the integrating sphere method we found that the bandgap of the $SnZrS_{3-x}Se_x$ does not obey Vegard's Law. Vegard's Law states that the lattice spacing will change linearly as the composition changes from one alloy to another [16]. It is widely accepted that with the change in the lattice spacing you get an inverse change in the bandgap energy. The lattice spacing of the $SnZrS_{3-x}Se_x$ system changes linearly for all three axes as the mole fraction changes. Larach showed for ZnS_xSe_{1-x} the bandgap energy changes linearly with the change in mole fraction while ZnS_xTe_{1-x} changes quadratically with the change in mole fraction [17]. The lattice spacing of the ZnS_xTe_{1-x} system changes linearly with change in mole fraction as with the $SnZrS_{3-x}Se_x$.

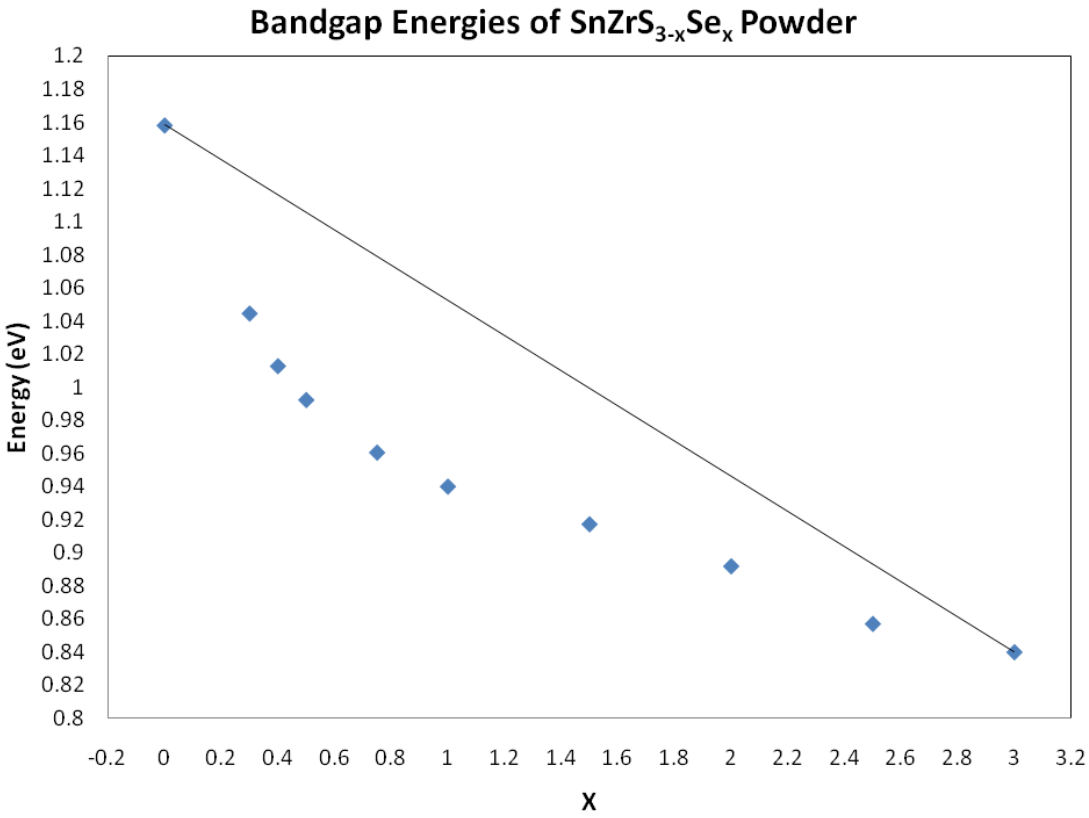

Figure 4.14: Optical bowing of the $SnZrS_{3-x}Se_x$ system. The bandgap energy drops down quickly when $x < 1$. While $x > 1$, the bandgap energy looks to change linearly.

Chapter 5 – Conclusion

The bifurcated fiber method for determining the bandgap energy of a powdered material has been shown to be as good as the integrating sphere method. The bifurcated fiber method collects a small solid angle near the normal of the powder sample, while the integrating sphere collects the total solid angle. With this difference in the solid angle we still find the same diffuse reflectance spectrum and bandgap energies of the powder materials. If the sample's reflection is a mix of specular and diffuse, as with a single crystal, the bifurcated fiber method will collect the both specular and diffuse reflection. The integrating sphere only collects the diffuse reflection, the entrance port allows the specular reflection to exit the integrating sphere. The integrating sphere method is ideal for samples with a large specular reflection component. With this in mind the bifurcated fiber method should only be used with samples with a large diffusely reflecting component, most powders, and the integrating sphere can be used with powder, thin films, and single crystal samples.

Bibliography

[1] MIT Spectroscopy. The Era of Classical Spectroscopy. <http://web.mit.edu/spectroscopy/history/history-classical.html>, Aug. 2010.

[2] E. Hecht and A. Zajac. *Optics*. Addison-Wesley Pub. Co., Reading, Mass., 1987.

[3] Y. Hishikawa, N. Nakamura, S. Tsuda, S. Nakano, Y. Kishi, and Y. Kuwano. Interference-Free Determination of the Optical Absorption Coefficient and the Optical Gap of Amorphous Silicon Thin Films. *Japanese Journal of Applied Physics*, 30:1008, 1991.

[4] D. McIntyre. (thin film optics.

[5] P. Kubelka and F. Munk. Ein Beitrag zur Optik der Farbanstriche. *Zeitschrift fur Technische Physik*, 11a:593601, 1931.

[6] B. Walter. *Ann. Physik*, 36:502, 1889.

[7] S. K. LOYALKA and C. A. RIGGS. Inverse Problem in Diffuse Reflectance Spectroscopy: Accuracy of the Kubelka-Munk Equations. *APPLIED SPECTROSCOPY*, 49:1107, 1995.

[8] J. Franklin. *Classical Electromagnetism*. Pearson Addison Wesley, 2005.

[9] P. Y. Yu and M. Cardona. *Fundamentals of Semiconductors*. Springer, 2001.

[10] *(HR4000 and HR4000CG-UV-NIR Series High-Resolution Fiber, Optic Spectrometers: Installation and Operation Manual.*

[11] Ocean Optics. HR4000 Spectrometer with Components. Online Image, March 2010. HR4000 and HR4000CG-UV-NIR Series High-Resolution, Fiber Optic Spectrometers: Installation and Operation Manual.

[12] Ocean Optics. *Near Infrared Spectrometer Installation and Operation Manual*, Apirl 2010. <http://www.oceanoptics.com/technical/nirquest.pdf> Manual no longer avaible online. Access hard copy.

[13] Ocean Optics. *Deuterium-Halogen Light Source*, April 2010. <http://www.oceanoptics.com/technical/dh2000.pdf>.

[14] S. López, S. Granados, and A. Ortíz. Spray Pyrolysis Deposition of Sn_2S_3 Thin Films. *Semiconductor Science and Technology*, 11:433, 1996.

[15] E. W. Ciurczak, R. P. Torlini, and M. P. Demkowicz. Determination of particle size of pharmaceutical raw materials using near-infrared reflectance. *Spectroscopy*, 1:36, 1986.

[16] A. R. Denton and N. W. Ashcroft. Vegard's Law. *Physical Review A*, 43(6):3161, 1991.

[17] S. Larach, R. E. Shrader, and C. F. Stocker. Anomalous Variation of Band Gap with Composition in Zinc Sulfo- and Seleno-Tellurides. *Physical Review*, 108(3):587589, 1957.